Localized Deformation Investigation in Irradiated Materials via Electron Microscopy and In Situ Testing

Maxim Gussev
Philip Edmondson
Gabriel Meric de Bellefon
Brian Eckhart
James Dixon
Keith Leonard

September 2017

OAK RIDGE NATIONAL LABORATORY

MANAGED BY UT-BATTELLE FOR THE US DEPARTMENT OF ENERGY

Fusion and Materials for Nuclear Systems Division
Materials Science and Technology Division

LOCALIZED DEFORMATION INVESTIGATION IN IRRADIATED MATERIALS VIA ELECTRON MICROSCOPY AND IN SITU TESTING

Maxim Gussev
Philip Edmondson
Gabriel Meric de Bellefon (University of Wisconsin–Madison)
Brian Eckhart
James Dixon
Keith J. Leonard

Date Published: September 2017

Prepared under the direction of the
U.S. Department of Energy
Office of Nuclear Energy
Light Water Reactor Sustainability Program
Materials Aging and Degradation Pathway

CONTENTS

LIST OF FIGURES

LIST OF TABLES

ABBREVIATED TERMS

bcc	body centered cubic
BSE	back scatter electron detector
CAD	computer-aided design
CIR	Cooperative IASCC Research program
CNC	computer numeric control
dpa	displacement per atom
EBSD	electron back scatter diffraction
EDM	electric discharge machine
EDS	energy dispersive x-ray spectroscopy
fcc	face centered cubic
FEG	field emission gun
FIB	focused ion beam
FIB-SEM	focused ion beam scanning electron microscope
GROD	grain reference orientation deviation
GSAS	General Structure Analysis System
hcp	hexagonal close packed
HR-EBSD	high-resolution electron back scatter diffraction
IASCC	irradiation-assisted stress corrosion cracking
IPF	inverse pole figure
IQ	image quality
KAM	kernel average misorientation
LAMDA	Low Activation Materials Development and Analysis
LWR	light-water reactor
LWRS	Light-Water Reactor Sustainability Program
ORNL	Oak Ridge National Laboratory
RHAB	random high-angle boundary
ROI	region of interest
RT	room temperature
SEM	scanning electron microscope/microscopy
SEM-EBSD	scanning electron microscopy electron back scatter diffraction
SNS	Spallation Neutron Source
STEM	scanning transmission electron microscope

EXECUTIVE SUMMARY

This report documents the experimental results of the in situ mechanical testing of irradiated austenitic stainless steels—materials of Light Water Reactors. The experiments were performed at Oak Ridge National Laboratory using Low Activation Materials Development and Analysis (LAMDA) and Spallation Neutron Source (SNS) facilities. The report is divided into sections that describe specific aspects of the in situ mechanical testing.

Section 1 reviews the background, motivation, and advantages of the in situ mechanical testing reported here and describes the equipment (i.e., scanning electron microscope, FEI Company's Versa 3D scanning electron microscope [SEM], and tensile stage) available at the LAMDA facility for working with irradiated specimens. Section 1 also describes the production of irradiated specimens at LAMDA. In-house specimen production is very important because it allows for more tests to be conducted, for additional statistics, and for secondary use of the valuable irradiated materials left over from previous projects. It also offers a decrease in specimen delivery time compared to offsite vendors, flexibility in geometries, and reduction in the specimen price.

Section 2 focuses on the methodological aspects of the in situ testing; this was an important topic to explore before testing valuable irradiated specimens. Nonirradiated specimens of two different 304L steel heats were tested in situ using scanning electron microscopy-electron back scatter diffraction (SEM-EBSD). The results on misorientation evolution, texture, and active deformation mechanisms such as dislocation slipping and twinning are discussed with regard to the electron beam current. The key finding of this section is the role of beam current in the strain-induced processes and phenomena occurring during the in situ mechanical test.

Section 3 is devoted to the in situ mechanical testing at the SNS facility; this experiment was performed in collaboration with University of Wisconsin–Madison and Gabriel Meric de Bellefon was funded under a DOE Integrated University Program Graduate Fellowship. Compared to the in situ SEM-EBSD testing, the neutron diffraction approach allows data collection to be performed for the bulk material; however, both methods (i.e., SEM-EBSD and neutron diffraction measurements) should be considered complementary. The section describes specimen geometry and preparation and peculiarities of mechanical testing at SNS and presents results on the load partitioning, diffraction peak broadening, and elastic strain analysis in the 10.9-dpa irradiated austenitic steel. The results highlight the pronounced difference between irradiated and nonirradiated steels regarding the mechanical behavior of different grain families, defect accumulation, and strain localization.

Section 4 presents the experimental results of the pilot SEM-EBSD in situ tensile experiment with the irradiated austenitic steel specimen. The experiment yielded a rich outcome on the deformation localization and strain-induced phenomena at different strain levels. Several selected regions of interest were tracked from zero stress through elastic and small plastic strains to the appearance of the well-developed neck. Because the same area was analyzed at different strain and stress levels, the collected EBSD data sets and corresponding SEM images allow for detailed analysis of relationships among dislocation channels, local misorientation level, and texture evolution. As expected, the results will be used later in the corrosion tests involving electrochemical microscopy.

The conclusion to this report summarizes the work performed and discusses future possible activities within the line of research.

1. IN SITU MECHANICAL TESTING

1.1 MOTIVATION

Materials in nuclear power plants are exposed to a harsh environment that combines stress, temperature, and radiation fields with transmutation effects. All these factors stimulate multiple degradation modes, including radiation hardening and embrittlement, radiation-induced segregation, swelling, and helium and hydrogen accumulation. Because of intensive research in the area of radiation-induced material degradation and the development of new materials, some damage modes have been successfully mitigated or are, at the very least, understood well enough to be controlled.

Nevertheless, several negative phenomena continue to influence the performance of in-reactor materials. For example, irradiation-assisted stress corrosion cracking (IASCC) is recognized as a critical concern associated with austenitic steels (e.g., 304L and 316L), which are widely used in the light-water reactor (LWR) operating environments [1–4]. Even though several new materials have come into use, the 300-series steels are expected to remain in service for at least the next 20–30 years, if not longer. As the existing fleet of LWRs ages, the IASCC-related issues are expected to become more severe. Consequently, this aspect is under active investigation by the Light-Water Reactor Sustainability (LWRS) program.

IASCC is a complex process involving many contributing factors, including microstructural and microchemical changes induced by irradiation [1–4]. At a high-damage dose (i.e., 20–40 dpa), stress corrosion cracking in 300-series steels may occur even in a low-potential corrosion environment, where a very low crack-growth rate was observed in nonirradiated or low-dose irradiated materials [2]. Recently, a close connection between plastic-strain localization (i.e., dislocation channeling) and IASCC susceptibility was recognized [3,4], with dislocation channels having an important role in crack initiation [3].

Systematic research of strain localization in irradiated austenitic steels, performed in the framework of the LWRS program, revealed the overwhelming complexity of this phenomenon. Several specific irradiation-induced deformation mechanisms were found and investigated [5,6], including the appearance of strain-induced martensitic phases associated with dislocation channels [6] and the formation of specific areas with high local misorientation called deformation "hot spots" [5]. Other researchers demonstrated the role of dislocation channels as stress localization sites [7].

At the same time, the experiments revealed limitations of the postmortem (or posttest) analysis. For example, the structure of the specimen with and without applied external stress may be not the same. While minor differences in the dislocation structure may be neglected, elastic strains in the austenitic steels after irradiation may be high enough to provide the driving force for structure evolution during unloading. It means that strain and stress distribution on the grain level may be different depending on the external loading conditions. This aspect is also important and worth investigating. Additionally, postmortem analysis provides only one point per area or specimen and does not allow for the kinetics of the process. With the in situ straining capability, one continuously deformed specimen will be able to provide data for a wide range of conditions (e.g., strain levels). This approach was successfully used for in situ creep experiments [8] and precise strain and misorientation mapping [9].

Thus, it is important to be able to characterize the structure continuously in situ. In the past, in situ testing required special equipment, expensive or just not available. Recent progress in experimental techniques allows for precise Kikuchi diffraction or electron back scatter diffraction (EBSD) measurements to be made inside a typical scanning electron microscope (SEM), which greatly enhances the available experimental capabilities.

EBSD has developed into a very useful tool, with high-resolution EBSD (HR-EBSD) coming into practical use several years ago [10]. Because EBSD patterns are sensitive to the elastic strains, HR-EBSD allows for direct measurements of the acting stress and for calculating the geometrically necessary dislocation density [10]. In a metallic polycrystal, local acting stress may be different from the applied macroscopic stress because of elastic anisotropy. Moreover, when measuring the sample under stress, one can find stress concentration points and connect them to structure features like grain boundaries and triple junction points [9,10]. Currently, a limited number of publications are available for nonirradiated materials, but practically no work has been done for irradiated materials.

EBSD analysis works only with the specimen surface; the volume cannot be analyzed without destroying the specimen. The neutron diffraction tool, VULCAN diffractometer, is available at the Oak Ridge National Laboratory (ORNL) Spallation Neutron Source (SNS) facility to investigate bulk materials. The in situ neutron diffraction approach is a powerful and complementary addition to SEM-EBSD in situ testing. To harness these and other potential benefits, the in situ mechanical capability at ORNL's Low Activation Materials Development and Analysis (LAMDA) laboratory is being developed.

1.2   THE LIBRARY OF IRRADIATED MATERIALS: CONCEPT AND CURRENTLY AVAILABLE ALLOYS

The LAMDA facility has assembled a library of irradiated materials from both active and completed programs. For example, the inventory of available specimens includes irradiated materials, including more than 12 austenitic alloys produced as part of the Cooperative IASCC Research (CIR) program [11], which was active between 1996 and 2010. The CIR samples were irradiated in the BOR-60 reactor, and details on this irradiation campaign may be found in [12]. As expected, the legacy materials from the CIR and other programs may serve as a source of irradiated 304L and 316L steels due to well-documented history. Additionally, several highly irradiated samples of 304L steel were purchased recently by the LWRS program. The samples—thin plates with a dimension of ~12 × 12 × 0.5 mm—were cut from bulk hex blocks that were irradiated at a maximum dose of ~35 dpa in the EBR-II fast reactor. The samples were delivered at LAMDA in March 2017 and will be used in further testing.

1.3   EQUIPMENT AVAILABLE AT LAMDA

1.3.1   Modern Advanced SEM

The microscopy area of ORNL's LAMDA laboratory is equipped with two scanning transmission electron microscopes (STEMs) and three dual-beam focused ion beam SEM (FIB-SEM) instruments.

One of these dual-beam FIB-SEM instruments—the Versa 3D SEM (Figure 1)—is a high-resolution imaging and analysis instrument. The instrument shown is equipped with a Schottky field emission gun (FEG) atop an electron column that can accelerate the generated electrons to energies of between 200 eV and 30 keV, with the ability to reduce the beam energy to 50 eV using beam deceleration. In imaging mode, the ultimate resolution of this instrument is 1.0 nm at 30 keV, although 0.8 nm point-to-point resolution is attainable using a STEM detector. Several electron detectors for imaging are available on this instrument, including an Everhard-Thornley detector, an in-column secondary electron detector, a back scatter electron (BSE) detector, and a STEM detector.

Figure 1. General view of the Versa 3D SEM.

In addition to high-resolution imaging capabilities, the Versa SEM also has the option to operate in an analytical mode in which high electron beam currents (>4 nA) are achievable. Two detectors, an energy dispersive x-ray spectroscopy (EDS) detector, and an EBSD, are installed on the Versa, which utilizes these high-beam currents for detailed characterization of the local surface chemistry and phase analysis. The EDS detector is an Oxford Instruments $X\text{-}Max^N$ with a 150-mm^2 solid-state detector. This detector provides quantitative and qualitative chemical information for most elements from uranium down to lithium. The EBSD system is based around an Oxford NordlysMax^2 high-efficiency platform for high-speed data acquisition. Both the EDS and EBSD are operated through the Oxford Aztec software system and can be operated independently or in parallel.

The Versa 3D SEM was selected to perform the in situ testing of the tensile stage because of its superior imaging and analytical capabilities. As such, the tensile stage was designed with this platform in mind.

1.3.2   Miniature Tensile Stage for In Situ Testing

After analyzing the available market options, Kammrath and Weiss Technologies, Inc. (https://www.kammrath-weiss.com) was chosen as the supplier for the miniature tensile stages. Kammrath and Weiss specializes in the development and production of custom-made systems for mechanical testing under specific conditions (e.g., vacuum, high or low temperatures, corrosive environments).

The purchased tensile frame (model MZ.Sb, shown in Figure 2) was delivered and installed in the VERSA SEM in December 2016. Several trial in situ tests conducted inside the VERSA SEM demonstrated that the working distance (i.e., the distance between the sample and the electromagnetic lens) might be as small as ~15 mm, which provides good resolution and a high-quality EBSD pattern. The tensile frame has a maximum loading capacity of 5 kN and a maximum strain rate of 50 µm per second (3 mm per min). Two force sensors—one with a 5-kN range and one with a 2-kN range—were ordered to support testing of miniature tensile specimens for the ongoing projects and to conduct mechanical fracture tests in the future.
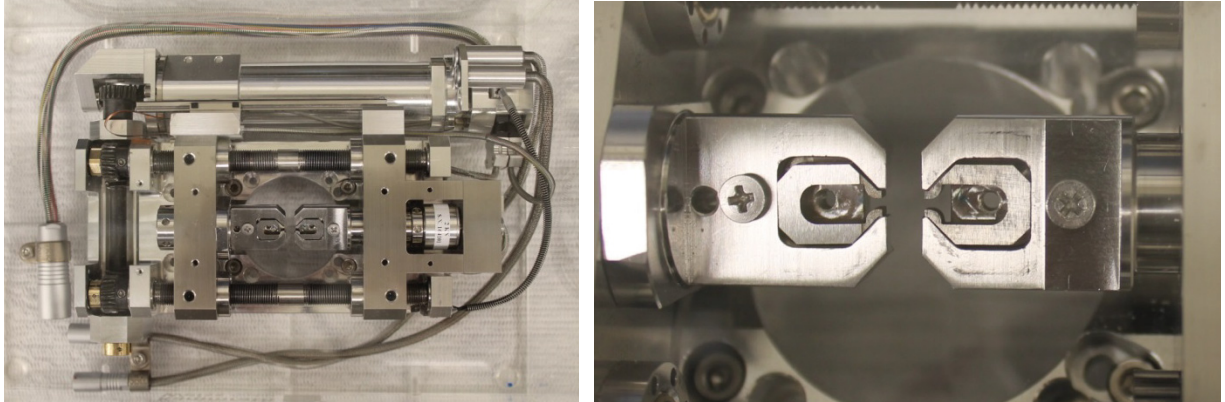
Figure 2. (Left) General view of the selected tensile stage frame. (Right) the enlarged image of the grips with holders installed for SS-J specimen geometry.

The selected heating stage (Figure 3) allows for a maximum temperature of 800 °C in a vacuum (or ~400 °C in open air, outside the SEM). Preliminary tests demonstrated the system's stability at elevated temperatures and low thermal inertia. However, implementing high-temperature testing will require additional careful work to ensure a uniform temperature field across the specimen gauge; thus, only room temperature experiments have been performed to date.
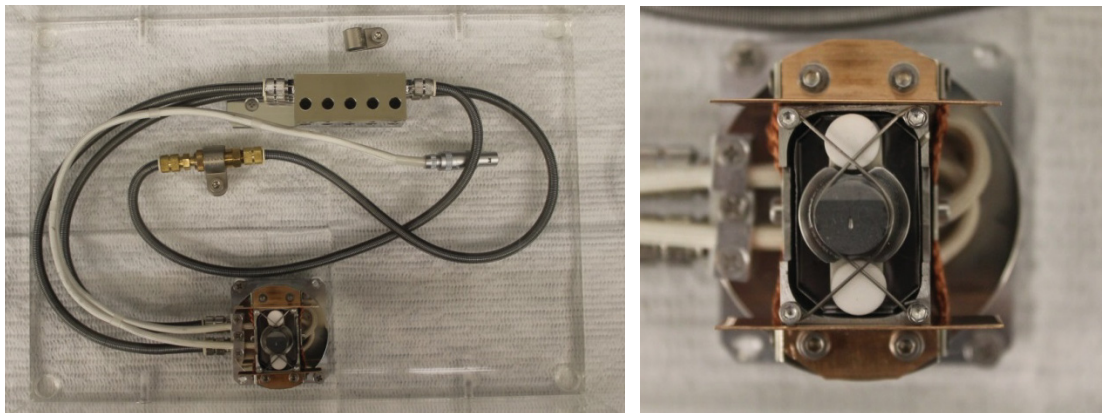
Figure 3. General view of the heater (left) and the enlarged view of the heating element (right).

Figure 4 shows the interior of the SEM chamber with the loaded tensile stage and inserted charge-coupled device camera; one may see very limited, confined space, which limits the availability of other instruments and detectors. For example, a BSE detector cannot be inserted; however, an EDS detector moving from the top should remain operational.

As shown in Figure 5, the system control units—computer, tensile stage controller, temperature controller, and water chiller—were mounted on the cart to provide a high degree of mobility.
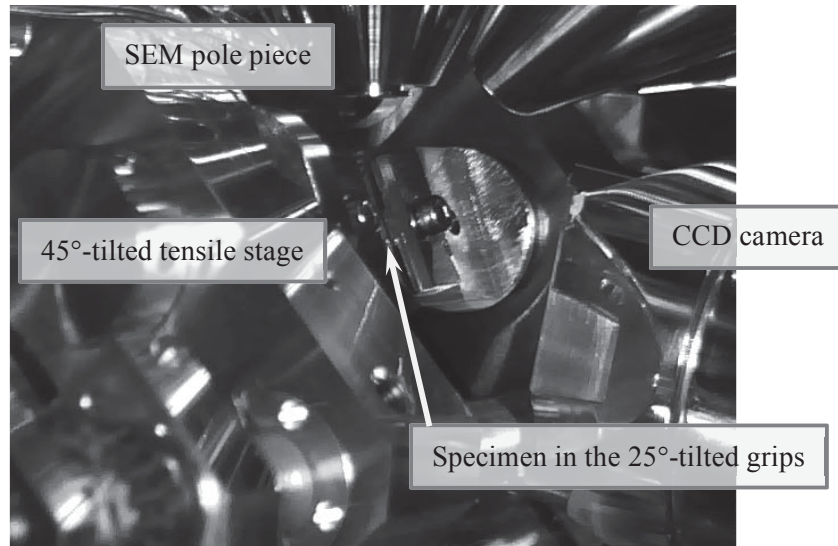
Figure 4. Interior of the SEM chamber with the loaded tensile stage and inserted CCD camera for recording EBSD patterns. The flat specimen surface is 70°-tilted with regard to the electron beam.
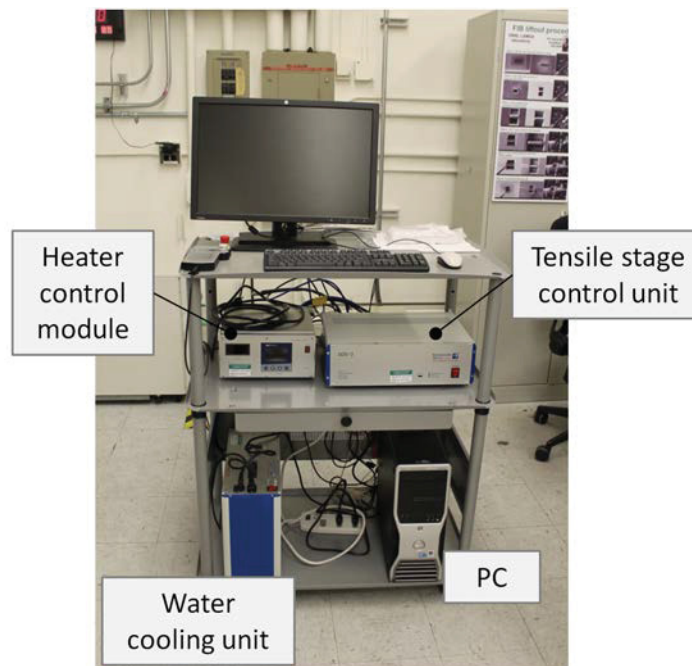
Figure 5. Tensile stage control modules located on the cart.

1.4   MANUFACTURING OF IRRADIATED SPECIMENS AT LAMDA

In-house production of irradiated specimens is an important capability because it allows for more tests to be conducted, for additional statistics, and for secondary use of the valuable irradiated materials left over from previous projects. It also offers a drastic decrease in the specimen delivery time compared to offsite vendors, great flexibility in geometries, and, in many cases, reduction in the specimen price.

However, taking into account the scientific value and cost of the irradiated material (e.g., high-dose austenitic steel), it is usually impractical to produce standard SS-3 or SS-J specimens in house. The shape and dimensions of the available irradiated objects (e.g., plates of ~7 × 3.5 × 1 mm) also often limit the possible specimen geometries. Thus, a miniature specimen design was developed to perform in situ SEM-EBSD tensile tests, Figure 6.

As expected, the geometry will accurately reproduce yield stress and ultimate stress for the standard, larger specimens like SS-J. Behavior at small strain levels should be comparable to the bulk specimens with larger work volume; however, the ductility level may be smaller compared to the SS-J geometry.
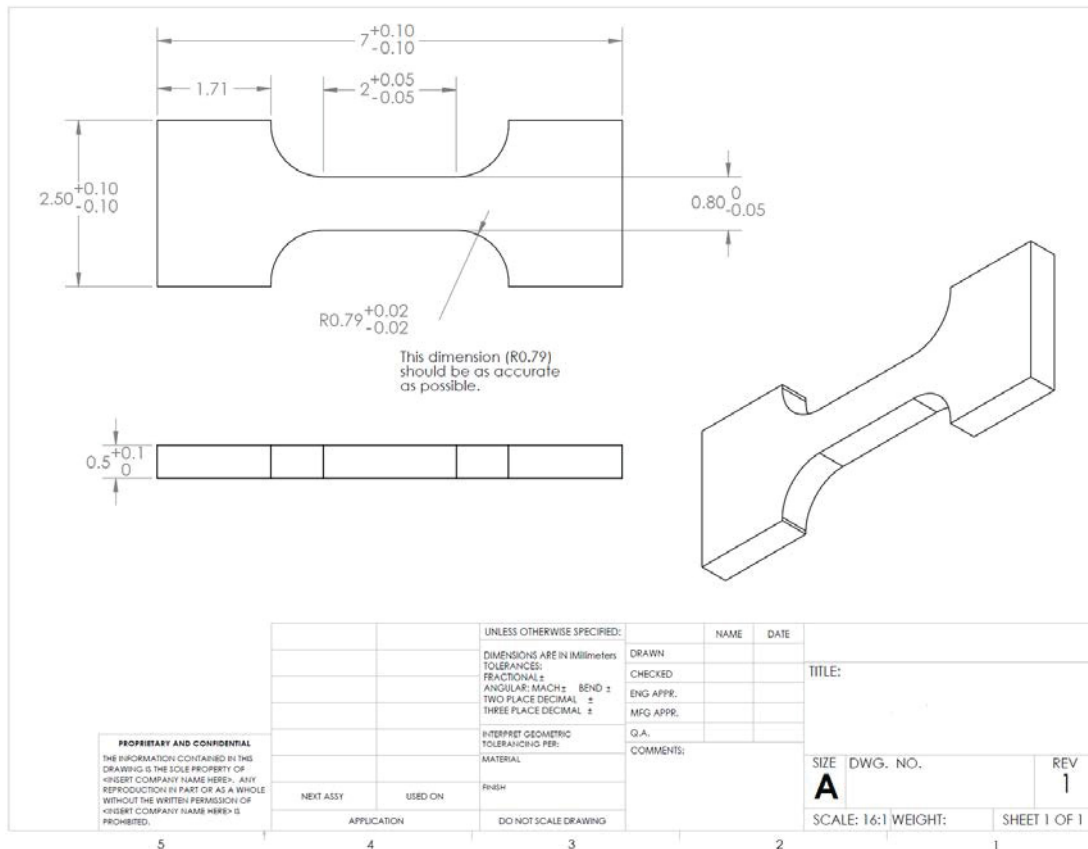
Figure 6. Geometry and dimensions of the ultraminiature specimen (SS-Tiny) for in situ testing.

Equipment (e.g., a milling machine) for manufacturing hot samples from previously irradiated materials should be simple to operate, easy to repair and replace, and affordable. At the same time, accuracy and reproducibility (at acceptable levels) are mandatory. The machine should also be small enough to fit a typical LAMDA hood. Specimen production should require minimum hands-on operations and be safe from a radiation control point of view.

After research and analysis of different machines on the market, a Sherline miniature 3-axis computer numeric control (CNC) machine (model 2010, shown in Figure 7) was purchased. The system passed all necessary safety control steps and had a certification from a Nationally Recognized Testing Laboratory. A computer-aided design (CAD) program was developed to produce a miniature rectangular "dogbone" specimen, shown in Figure 6. Total specimen length will be approximately 7 mm and may vary depending on the available material. After machining, specimen preparation to the in situ test may be

performed using standard procedures such as mechanical grinding and electropolishing. The CNC machine is easily programmed to produce virtually any tensile specimen geometry.

Material piece (5.5 × 3 × 1 mm) mounted on the aluminum holder plate.

Machining side A.
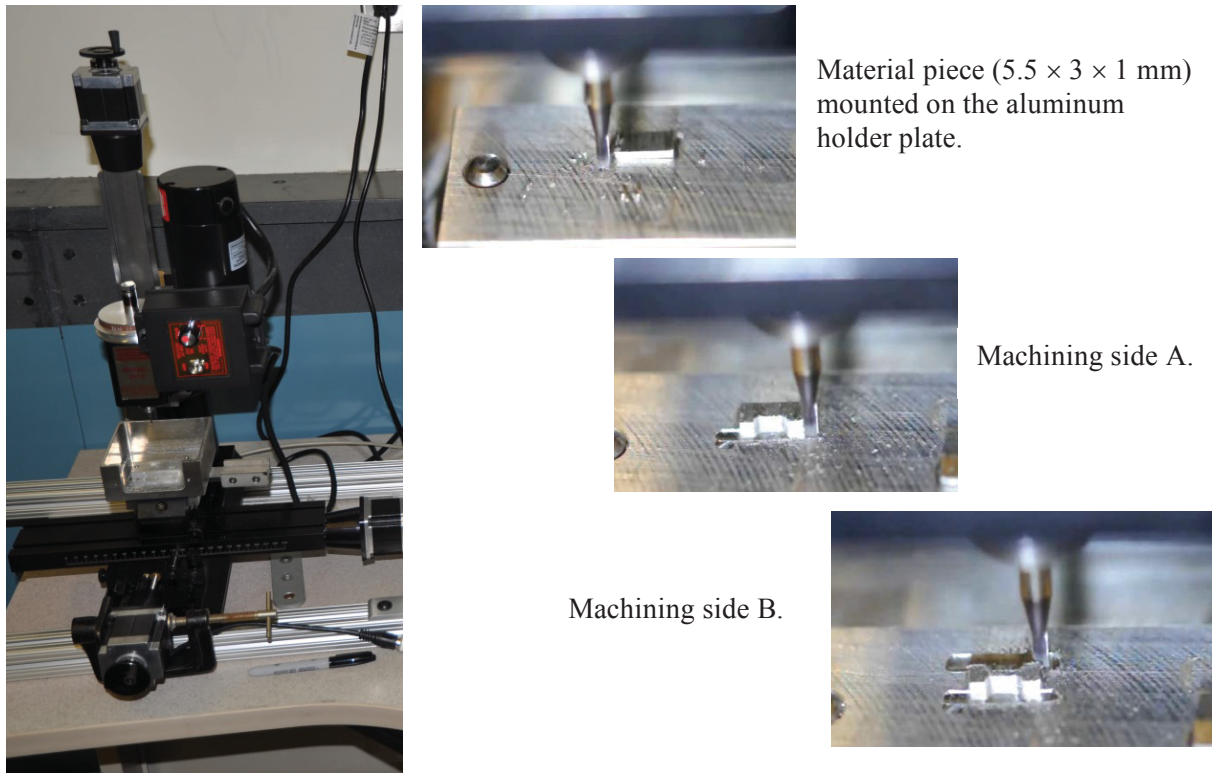
Machining side B.

Figure 7. CNC milling machine, model 2010 (left) and specimen manufacturing steps (right). Images of the machining are slightly blurry because this process is performed in a water-filled container.

1 mm
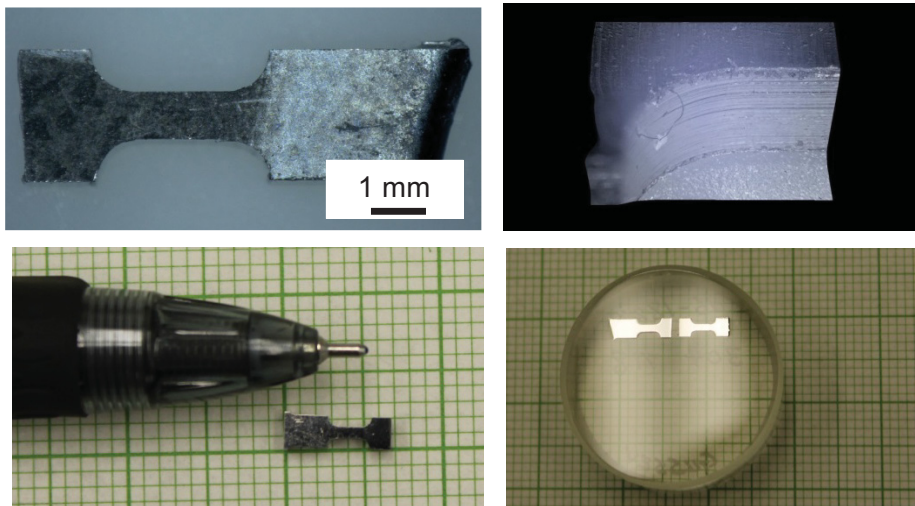
Figure 8. A 718-alloy miniature specimen (top left), a 3D-image of typical tool marks on the specimen edge (top right), and miniature specimens unmounted and mounted in epoxy (bottom).

Several test runs were conducted using 6061 aluminum alloy, annealed and cold-worked 304 steel, and—as a material with ultimate strength—precipitation-hardened 718 alloy. Promising results were obtained, and it was shown that 718-alloy could be used to produce a miniature tensile specimen (Figure 8) that

would have a yield stress of around 1200 MPa, which is above the maximum value expected for highly irradiated austenitic steel, ~1000 MPa.

After that, the CNC machine was installed in the hot area at the LAMDA laboratory. The first set of irradiated specimens (Figure 9) was produced in March–April, 2017, creating an opportunity for in-house in situ SEM-EBSD testing with irradiated materials.
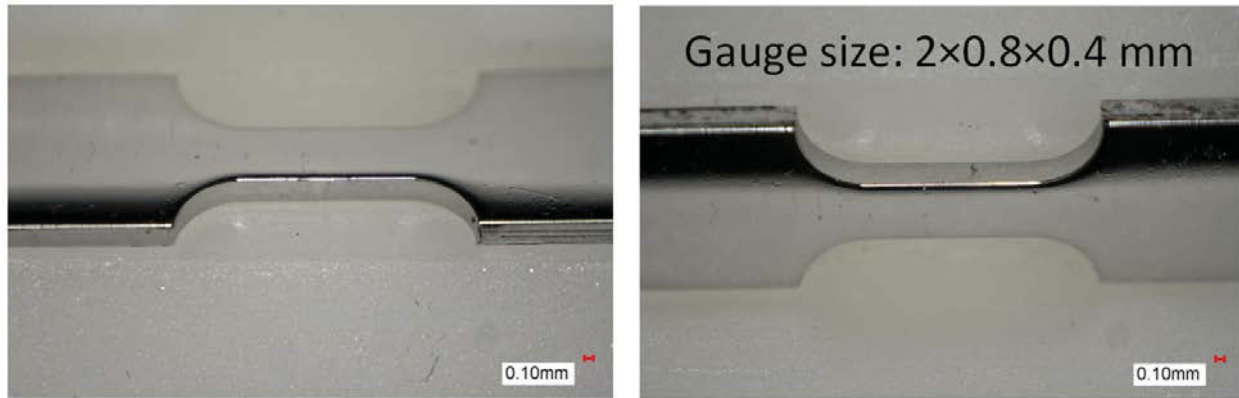
Figure 9. Miniature irradiated tensile specimens (SS-Tiny) manufactured at LAMDA. One would see a high-quality mirror-like surface quality after additional preparation via mechanical grinding and electropolishing.

1.5 CONCLUSIONS

The in situ SEM-EBSD mechanical testing approach used for the present work was established at ORNL's LAMDA facility for testing miniature irradiated specimens. If necessary, the tensile specimen may be produced from irradiated material in house, providing the researcher with additional freedom and flexibility in the experiment design.

2. CHALLENGES OF THE SEM-EBSD IN-SITU MECHANICAL TESTING

2.1 INTRODUCTION

In situ mechanical testing—continuous or step-by-step deformation while measuring material parameters and evaluating strain-induced changes—is a powerful modern research technique. Usually, in situ testing combines mechanical loading and deformation in elastic or elastic-plastic mode(s) with diffraction measurements (neutrons and X-rays) [13–15], X-ray tomography [16], or EBSD scanning [17,18], allowing for the investigation of features such as lattice strains, grain rotation, texture evolution, and crack advance. Using a single specimen, it may be possible to derive data for a broad range of stress and strain levels for the same area or volume. Reducing the number of specimens to be tested may be of special importance if the material is of high value, dangerous, or both (i.e., neutron-irradiated high-dose specimens).

EBSD analysis—and especially its recently emerged version, HR-EBSD—seems to be one of the attractive analytical techniques for use during in situ testing because EBSD provides crystallographic information for a wide range of scales (from hundred nanometers to millimeters) and has a high degree of flexibility regarding scan resolution and accuracy (e.g., step or pitch size, camera binning [19]). HR-EBSD allows for measuring the density of geometrically necessary dislocations [20] and for estimating elastic strains and acting stresses by analyzing high-quality patterns in the offline mode [21].

However, in situ tensile testing often raises questions regarding the influence of the selected experimental approach on the processes in the material. Is there a possibility to introduce artifacts by unloading or aging the specimen between the steps or by scanning the region of interest (ROI), in this case the gauge region of the tensile bar? Answering this question is important if the material of interest reveals several deformation mechanisms or strain-induced phenomena, which are sensitive to the temperature, surface conditions, and stress, or if the deformation mechanisms are expected to be sensitive to the material history. For example, dislocation slip mode (e.g., multiple slipping or channeling), twinning, and phase instability, among others, may be influenced by annealing or aging, texturing [22], or irradiation conditions [23].

The present work included performance of in situ tensile tests with 304L austenitic steel. Austenitic 300-series steels are widely used in industrial applications, including nuclear energy, due to good mechanical and corrosion properties, processability, weldability, and affordability. However, these steels also suffer from a number of common issues such as stress corrosion cracking [24], radiation-induced swelling [25], and second-phase formation and evolution during aging [26]. The practical importance of these materials continuously attracts researcher attention [17,18,23,27]. In the context of the present work, it is important that 304L steel reveals deformation twinning and phase transformation phenomena [18,23]; minor variations in the composition may control the rate and effectiveness of these processes. Additionally, phase and structure transformations may be enhanced by irradiation influencing material ductility [27] and other performance metrics.

The combination of practical importance and multiple strain-induced phenomena makes this steel the best choice for many purposes. Here, in situ mechanical testing was conducted inside a SEM using EBSD analysis, revealing some results that may be regarded as challenges compromising the in situ testing approach.

2.2   MATERIALS FOR TRIAL TESTING

Two 304L steel heats were investigated to establish the limits and boundary conditions for in situ tensile test experiments. The first material, a nuclear-grade, high-purity AISI 304 austenitic stainless steel, had an annealed austenite structure with zero retained ferrite amount and an average grain size of around 57 μm. Due to the relatively high Ni content (10.45%), the material was expected to have limited phase transformation intensity with pronounced deformation twinning. This particular heat was considered a reference for the commercial steel irradiated in fast [28] and power water reactors. The in situ testing of the irradiated specimen is described in Section 4 of this report.

The second material, a commercial 304L steel, had an average grain size of approximately 45 μm, and the structure contained ~2% of the retained ferrite; the retained ferrite amount varied slightly, within ±1–1.5%, depending on the location. This heat was selected to serve as a surrogate material for the hex-block specimens purchased recently (see Section 1.2). Efforts to obtain the actual reference archive material for the hex-block specimens are in progress.

The element composition of both materials (Table 1) was verified by a commercial vendor. Both steels were within the formal 304 composition range, but the nuclear-grade version (high-Ni 304L) had an increased amount of Ni and a reduced amount of Si; the difference in other elements was not significant (Table 1).

Representative tensile curves for both materials are shown in Figure 10; yield stress values were close enough (~250 MPa), whereas steel #2 demonstrated some increase in the deformation hardening rate starting at a strain level of ~0.25–0.30 (~25–30%) due to the intensive martensitic transformation [29] and significantly larger uniform and full elongation values.

Table 1. Composition (wt %), grain size, and expected deformation mechanisms for the investigated materials

Alloy no.	Description	Fe	C	Mn	Si	Cr	Ni	Mo	N	Grain size (µm)	Expected deformation mechanisms
1	Nuclear-grade, high-Ni 304L	Bal.	0.016	1.03	0.24	18.39	10.45	0.0013	0.056	57	Dislocation slipping, twinning
2	Commercial low-Ni 304L	Bal.	0.020	1.28	0.450	18.29	8.02	0.074	0.054	45	Dislocation slipping, phase transformation

Ex situ EBSD analysis was conducted using a JEOL JSM 6500F SEM with an FEG equipped with an EDAX EBSD system. The accelerating voltage for the investigations was 20 kV, and the working distance was 12–17 mm. The step size of the EBSD maps varied between 0.5 and 3.0 µm depending on the resolution needed for microstructural assessment.

In situ mechanical testing was conducted using an FEI Versa 3D SEM, Figure 1, equipped with an Oxford Instruments Nordlys-2 EBSD system. The voltage was fixed at 20 kV, and nominal beam current values of 8 nA or 32 nA were used. Inaccuracy in the beam current value, as believed, did not exceed 10–15%. To perform the in situ mechanical testing, the microscope was equipped with a Kammrath and Weiss model MZ.Sb miniature tensile frame (Figure 2). The frame has a maximum loading capacity of 5 kN and a maximum strain rate of 50 µm per second. Tensile tests were conducted at a strain rate of $10^{-3}s^{-1}$; strain increment between the steps varied from ~4 to 6%. EBSD data collected during the in situ test were converted to the EDAX-compatible file format and processed using EDAX OIM v.7.2 software. Due to strain-induced relief formation, the noise level and the fraction of incorrectly indexed or nonindexed points were higher compared to the conventional ex situ scanning.
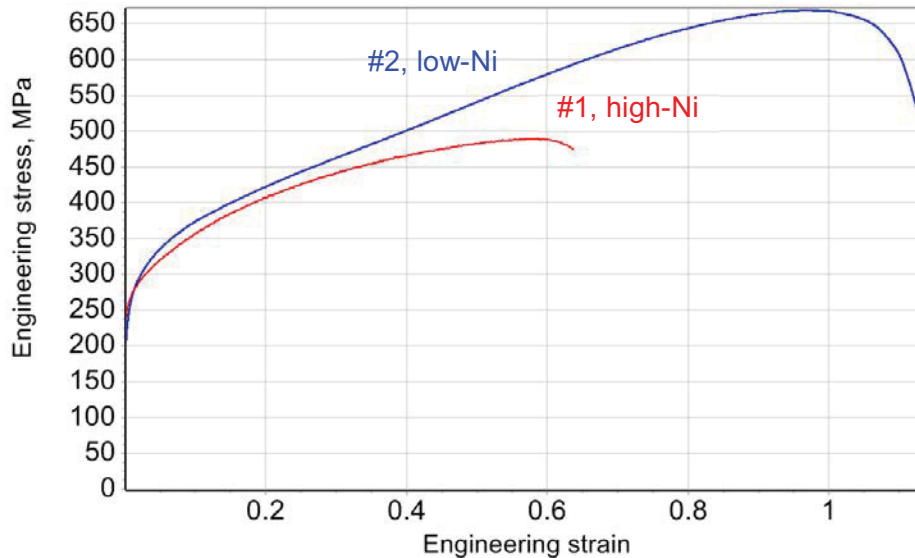
Figure 10. Representative engineering tensile curves for the studied materials.
Specimen geometry is shown in Figure 6. Geometry and dimensions of the ultraminiature specimen (SS-Tiny) for in situ testing.; specimen thickness was 0.4 mm. This miniature specimen was specifically designed to be used for irradiated material testing (Section 4).

Tensile specimens (Figure 6) were produced from the parent plates using an electric discharge machine (EDM). After EDM cutting, the 1-mm-thick specimen blanks were mechanically ground to fit the required thickness dimension. After that, the specimens were polished down using 3-μm diamond lapping paper and finally electropolished for 10 s using Struer A2 electropolishing solution and 30 V direct current. After preparation, the specimens had a mirror-like clean surface and a thickness of ~350-360 μm. It is important to note that this specimen geometry was designed to provide the tensile stress state during the in situ mechanical test and is not intended to deliver the mechanical property values comparable to other common geometries [30]. Whereas the yield stress for this geometry was comparable to massive specimens, ductility values may be different.

During deformation, local strain values at the specimen surface may be different from an externally applied nominal strain (often termed "global strain"). The difference is caused by deformation bands appearance and propagation, necking, material inhomogeneity, or reduced number of grains across the specimen thickness. To measure the local strain level, the same specific points (e.g., inclusions in the SEM images [Figure 11] or triple junction points in EBSD maps [Figure 12]) were used as fiducial marks and tracked through the data sets for all strain levels. The distance between the points, treated as a "virtual gauge," was used to calculate the local strain levels by analogy with [31]. For each ROI, five to seven gauges were evaluated, and an average strain value was reported in terms of engineering strain definition.

2.3   EXPERIMENTAL RESULTS

2.3.1   High-Ni 304L steel

Specimens were deformed in a step-by-step mode with a strain increment of ~4–5%. The SEM images (Figure 11) were taken at each strain level to analyze the surface evolution and estimate the local strain level. As strain increased, deformation-induced changes became clearly visible. A strong increase in the slip line density dominated at small strains; grain rotation and surface relief formation were evident at a few percent of strain. Figure 12 shows the evolution of the EBSD maps as the strain level increased. The EBSD data quality remained acceptable within small and moderate strain ranges (<20%). The preliminary tests were able to reproduce all specific strain-induced phenomena described in the literature [32]: grain rotation, grain fragmentation, and increase in in-grain misorientation. Grains with an initial orientation close to [101] rotated towards the [001]–[111] line, and their color changed in the inverse pole figure (IPF) map. In-grain misorientation increased significantly, leading to a strong increase in the Kernel Average Misorientation (KAM) values and formation of specific areas with increased KAM.
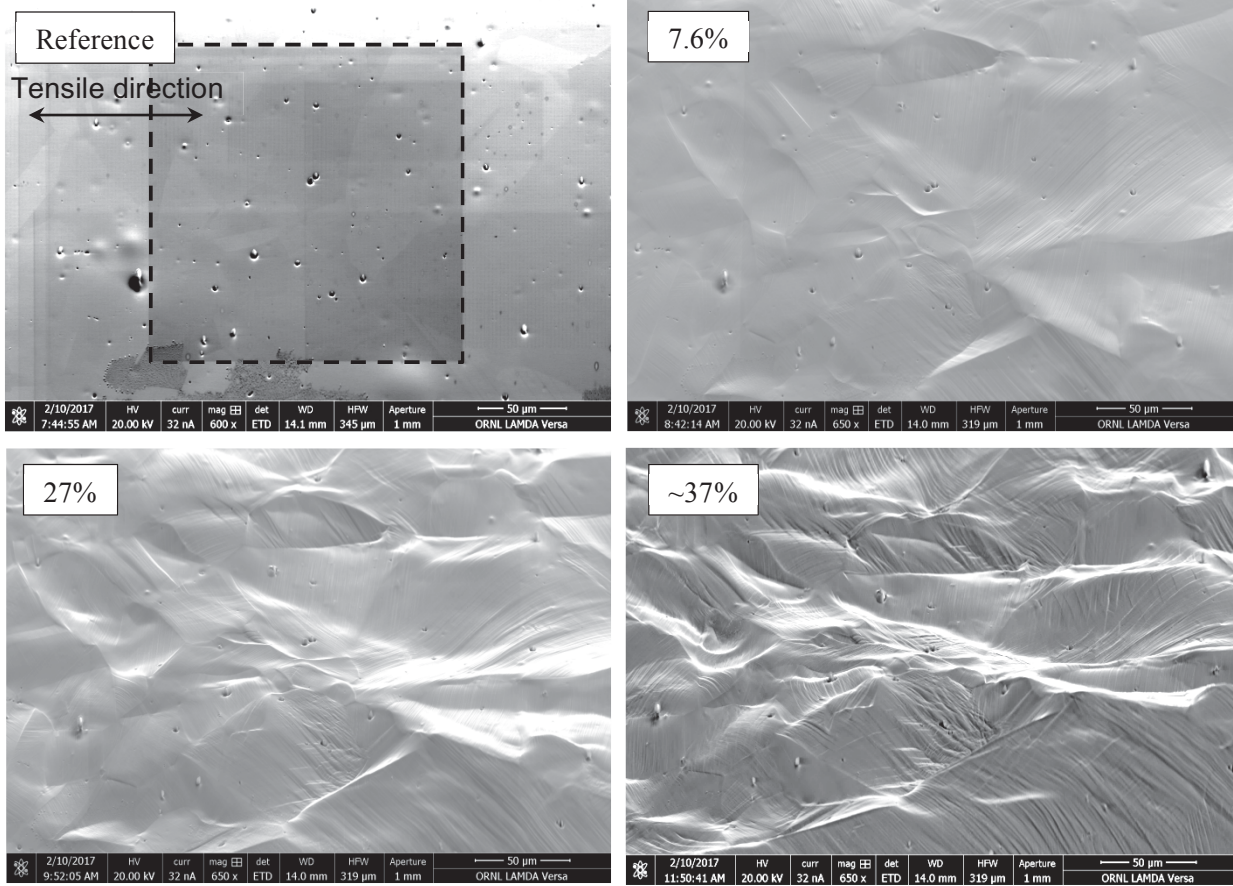
Figure 11. SEM images taken at different strain levels. These images demonstrate the surface topology evolution from single slip lines to multiple active slip systems and pronounced strain-induced relief. The dashed rectangle identifies the ROI for this particular specimen. Image magnification is the same throughout all images.

As the strain level increased, the EBSD map quality degraded drastically. At the local strain level of ~27%, many areas became invisible because of a shadowing effect caused by grain rotation and strain-induced roughness. Nevertheless, many grains still appeared well indexed in the resulting maps, which provided an opportunity to analyze processes at large strain levels.
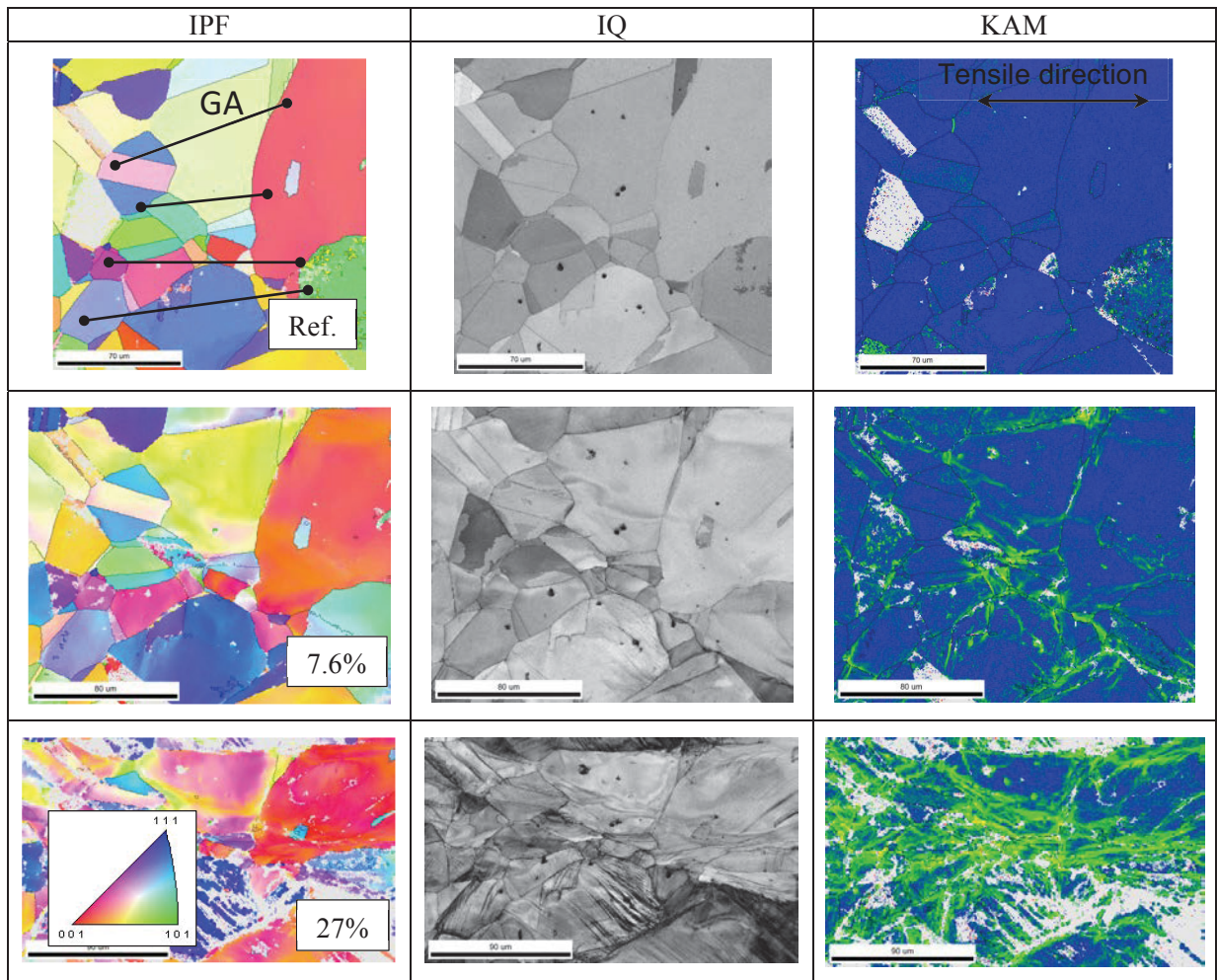
Figure 12. The representative EBSD data set for different strain levels; "Ref." designates the reference data set obtained at zero strain. Scanning was performed using 32 nA beam current. Strain values were calculated from SEM images taken at the same location using the same imaging conditions (i.e., working distance and magnification). The gauges (G) in the Reference IPF map illustrate the method for estimating local strain level (by analogy with [31]). The IPF color key is the same for all IPF maps in this report; the IPF maps here and below are colored in the tensile direction.

Figure 13 shows the EBSD data quality (i.e., the fraction of successfully indexed points) as a function of local strain level. As shown, most of the ROI was successfully scanned (>80% of the points of interest) at strain levels below 20%. When strain exceeded ~30–35%, the fraction of successfully indexed points dropped below 50%.
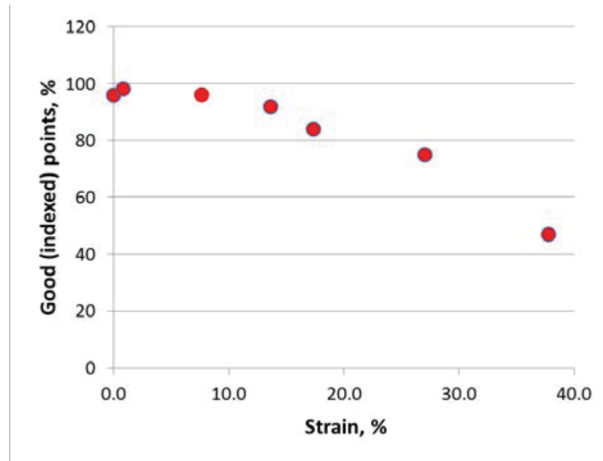
Figure 13. EBSD data quality as expressed by the fraction of "good points").

2.3.1.1 Analysis of EBSD strain metrics

The most common EBSD strain metrics—grain reference orientation deviation (GROD) and KAM—were calculated for the reference area shown in Figure 12. The maximum GROD values (i.e., the largest increase in the grain deviation from some reference value) increased linearly with the strain level. Starting at a strain level of ~15–17%, the maximum GROD values tended to saturate because of grain fragmentation and the appearance of in-grain boundaries within the grain. It appears that below this 15–17% strain level, the GROD maps may be used to estimate the local strain level if a sufficiently large area (~30–50 grains, or size of ~180 × 180 µm) is scanned. The KAM value also increased linearly with the strain level up to around 20% strain (Figure 14). After that, the KAM value continued to increase but at a slightly shallower rate/slope. The linear relationship between KAM and strain level agrees with the literature [19,33] and allows for estimating the local strain values at a given location if the reference value and the correlation curves are known [19,33].
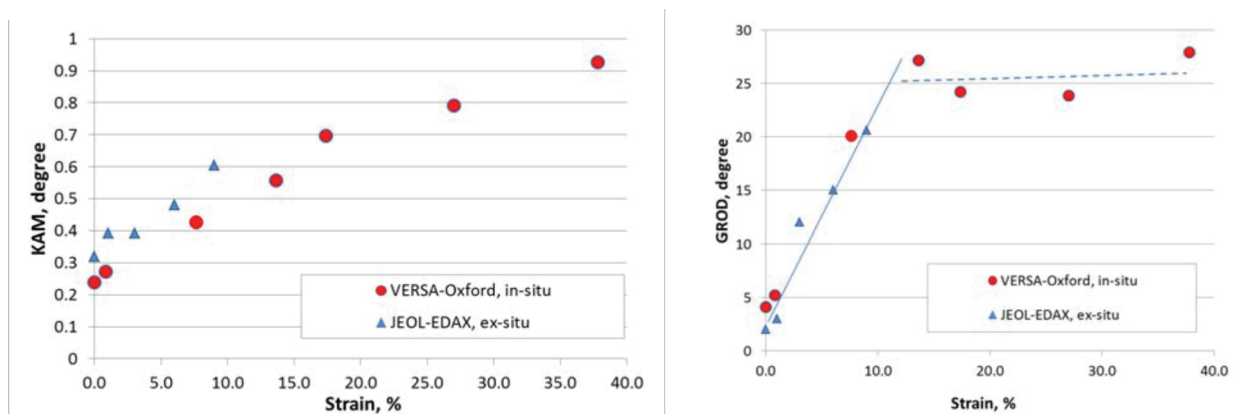
Figure 14. GROD and KAM as a function of local strain level. In situ data (round markers) are compared to ex situ test data (triangles); step size was the same for both at 0.5 µm. Scanning was performed using 32 nA beam current.

The in situ test results were compared to the ex situ tests performed earlier. In this case, a series of tensile specimens were deformed at room temperature and then EBSD scanned using a different system, the JEOL JSM 6500F SEM. As shown in the results (Figure 14), the strain-induced changes in the GROD parameter were close enough for both in situ and ex situ tests. The KAM parameter has a similar slope,

but the curve was slightly shifted up. Good agreement between the in situ and ex situ (i.e., postmortem) test results confirms the reliability of the EBSD data obtained on a single specimen deformed in step-by-step mode.

It is important to note that the GROD and KAM curves for the in situ test case were obtained from a single specimen, thus minimizing the number of required specimens for the experiment; sourcing multiple specimens of irradiated material can be prohibitively expensive. Furthermore, specific defect-to-defect interactions may be easily tracked with the in situ method.

2.3.1.2 Deformation twin appearance and evolution

Figure 15 shows an appearance and evolution of the deformation twin. The EBSD map (fragment of the general IPF map in Figure 12) demonstrates the twin-free grain at 13.6% strain (left column), the appearance of several strain-induced twins at 17.4% strain, and their growth coinciding with the strain level increase. Additionally, the IQ map with visible boundaries allows for a clear delineation between simple slip lines and areas containing deformation twins; the twins appear to be darker. In other words, the IQ maps provide an additional way to confirm the observed phenomenon (e.g., twinning). Strain and stress values required to initiate twinning may be defined more precisely, or at least more accurately, compared to the ex situ posttest analysis. Grain orientation regarding the external stress direction may also be easily
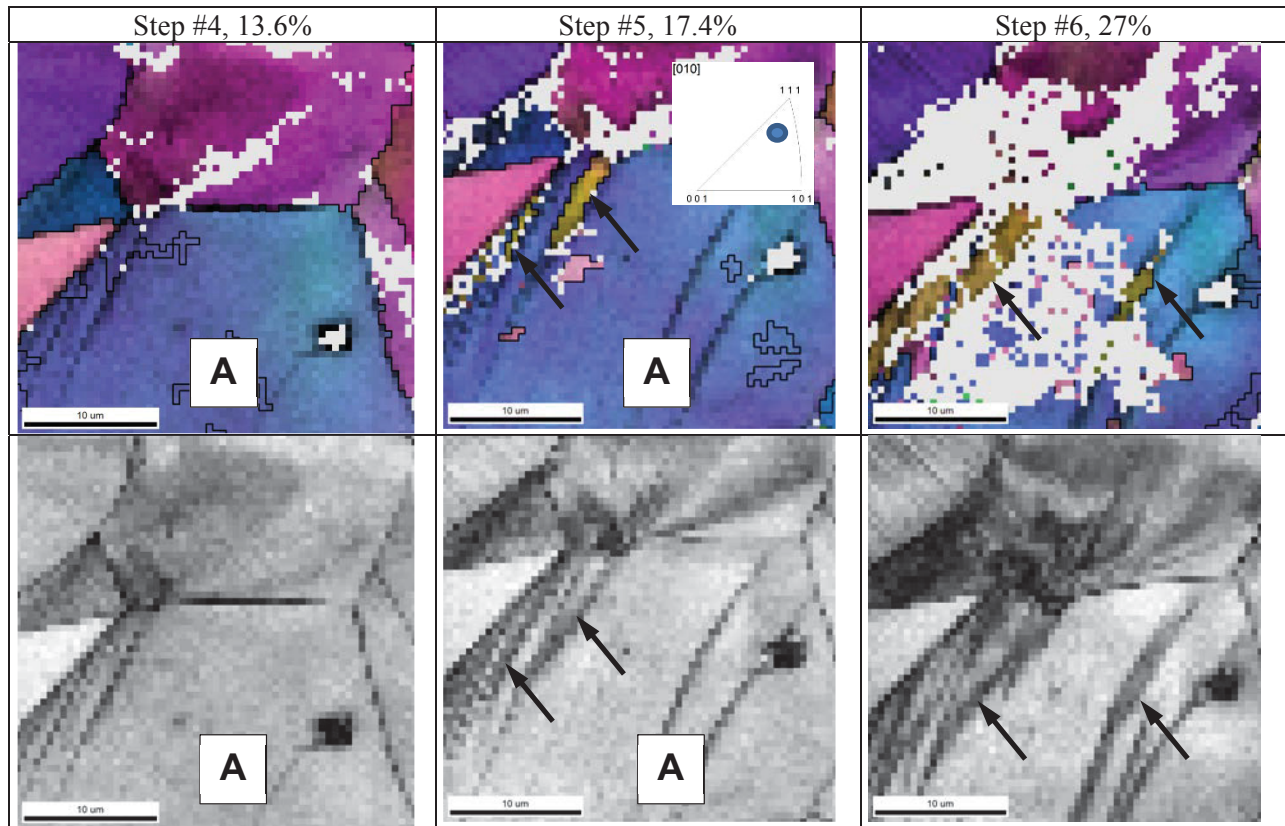
Figure 15. Deformation twin appearance and evolution. Grain A was twin free at 13.6% strain, and a clear indication of the strain-induced twin (marked by black arrows) appeared during the next strain increment (step #5, 17.4%). With another strain increment (Step #6, 27%), the twins grew, and an additional twin appeared in a different area. Note the strong increase in the nonindexed point fraction. Scanning was performed using 32 nA beam current with 0.5 μm step.
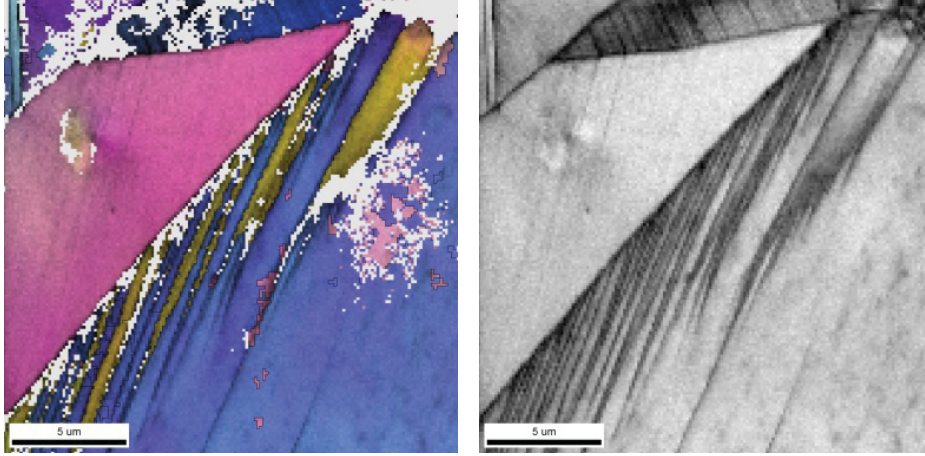
Figure 16. EBSD data for the area shown in Figure 15. Scanning was performed at 1500× magnification with a 125-nm pitch (Step 5, 17.4%). Shown are fine deformation twins in addition to the coarse deformation twins visible in the 0.5-µm scan. Scanning was performed using 32 nA beam current.

defined. If necessary, the ROI or its subregion may be scanned at an increased magnification and smaller step size to gain more detailed information. Figure 16 shows the same area as Figure 15, illustrating the complexity of twinning (e.g., multiple fine "needles" growing into the parent grain).

Deformation twins were observed during in situ testing at ~13.6–17.4% in the grain oriented close to the [111]-corner of the unit triangle, with respect to the tensile direction; the first deformation twin was observed in the bulk, ex situ tested specimen (not shown here) at 12% of strain in the [111]-oriented grain. One could conclude that in situ testing accurately reproduces twinning regarding strain level and grain orientation.

2.3.2 Low-Ni 304L steel behavior

Figure 17 shows the evolution of the annealed low-Ni 304L steel structure at small strain levels. The material contained two phases: dominating austenite face centered cubic (fcc) and a small amount of retained ferrite body centered cubic (bcc). Ferrite formed specific inclusions composed of small grains. An additional phase—strain-induced bcc-martensite, often referred to as α'-martensite—was observed at 5.3% of plastic strain; at ~10% martensite amount reached ~5-7%; this value agrees with [29] (i.e., ~9–11% at ~10% strain). Low-Ni concentrations greatly reduced the strain and stress levels required to initiate martensitic transformation. In ~7% Ni 304 steel, the critical strain level may be even smaller by up to a few percentage points [18].

The α'-particle of ~10-µm length formed near a grain boundary in the vicinity of the retained ferrite colony is shown in Figure 17b. The martensite particle had a darker color in the IQ map compared to austenite and retained ferrite, and martensite had clear visible dark boundaries. The clear visibility in the IQ map is an additional sign allowing for filtering false indications. As strain increased, several pronounced α'-colonies (C_α in Figure 17c) formed in the grains oriented close to [111] with regard to the tensile direction.

Interestingly, the appearance of the colonies was preceded by the formation of pronounced, highly visible slip lines in the IQ map at 5.3% of strain. Elongated α'-plates were often located close to the pronounced [111] slip lines; this observation agrees with [18]. The in situ results for the near-surface layer agreed well

enough with ex situ data for the bulk. First signs of the transformation appeared as ~5% strain, and the growing martensite colonies were observed at ~9% strain (not shown here).
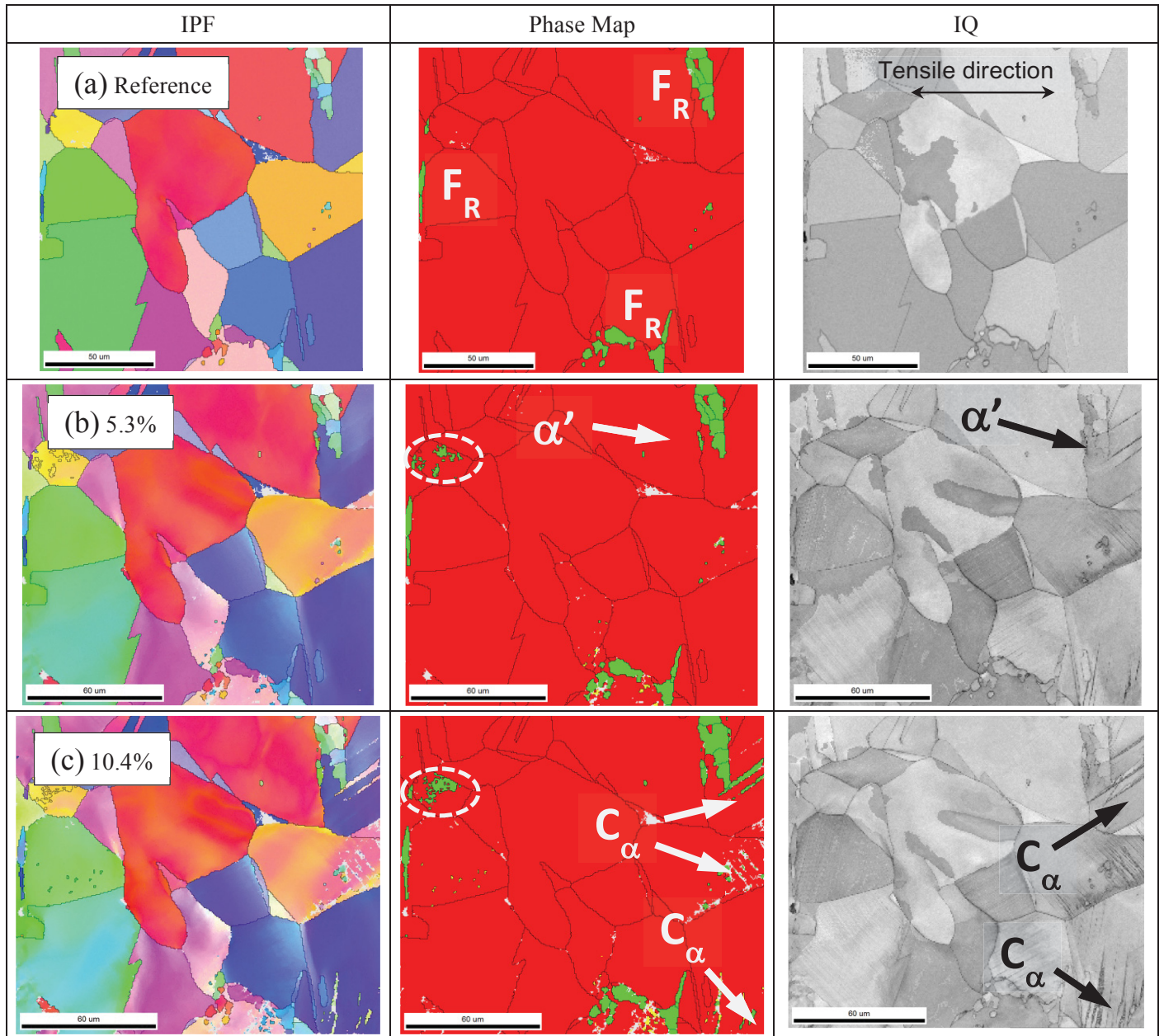
Figure 17. A typical ROI prior straining and at small strain levels in low-Ni 304L steel. Scanning was performed using 8 nA beam current. In the phase map, austenite is red; ferrite and α'-martensite are green. One may see retained ferrite (F_R) in the structure forming specific colonies. After the first step, a bcc-martensite particle appeared close to grain boundary (α' with arrows). After the second step, several additional martensitic colonies (C_α) appeared in the structure. The martensitic phase is clearly distinguishable from the retained ferrite. Several false indications are shown by dashed oval; note there are no strain-induced features in the corresponding grain in the IQ map.

Analyzing the IPF maps, one could deduce that martensitic transformation is sensitive to the grain orientation with regard to the acting stress direction [23]; local grain configuration, texture, and stress state may influence transformation kinetics. Additionally, strong variant selection exists and usually

parent austenitic grains contain 1 to 3 orientation variants among 24 possible [18]. However, these aspects are out of the present work scope and will not be discussed here.

As the experiment progressed, the α′-colonies grew, consuming the parent fcc-grains (Figure 18a). New martensite colonies formed whereas some grains remained transformation free. The analyzed martensite colonies consisted mainly of bcc-martensite; very weak indications of the hcp (hexagonal close packed) phase (ε-martensite) were observed during automatic scanning but not confirmed by manual analysis of the recorded Kikuchi patterns.

Scanning with 8 nA beam current provided data flow rate of ~20 Hz (points per second) and required ~2 h to scan the area of a minimally acceptable size (here ~150 × 150 μm with 15–20 grains). The increase in the beam current from 8 to 32 nA promised a scanning rate increase of up to ~80–100 Hz. It would allow for larger statistics, or for more fine strain steps, within the same time on the instrument. Additionally, larger currents usually produce better, higher contrast patterns. Thus, in situ testing with 32 nA current was conducted using the same 8%-Ni 304L steel specimens but yielded an unexpected result: Scanning the deformed structure revealed austenite (i.e., fcc) and retained ferrite (i.e., bcc) but no strain-induced martensitic transformation. First signs of the martensite appeared at unexpectedly high strain levels (~19.5% for the data set shown in Figure 18b) whereas the 8 nA scanned specimen contained well-developed martensite colonies starting at 12–15% and initials signs of transformation at ~5.3% (Figure 17).
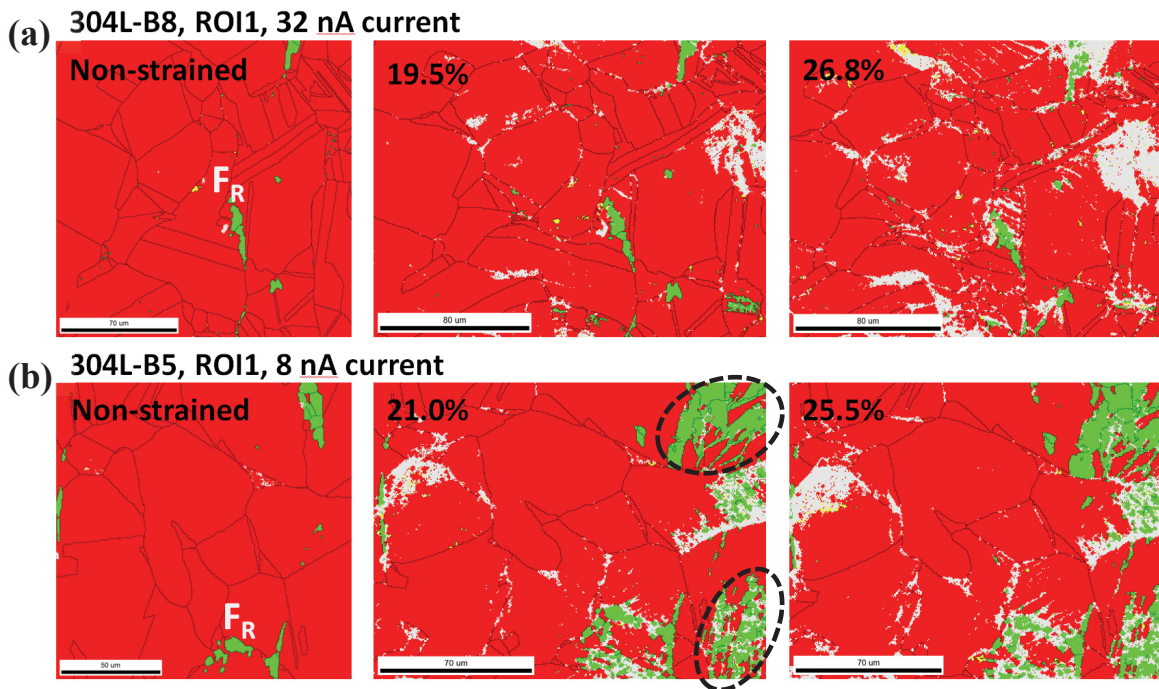
Figure 18. The difference in the phase transformation behavior between areas, scanned using 32 nA beam current and 8 nA beam current. Retained ferrite (F_R) is visible in the structure. The top phase map row (32 nA) shows very weak signs of the phase instability. Only a few small particles were observed. The bottom row (8 nA) demonstrates formation and evolution of dense and relatively large α'-colonies (dashed ovals). In the phase maps: fcc is red, bcc is green, and hcp is yellow; light-gray color shows nonindexed points.

A control experiment was conducted via scanning several closely located areas on the same tensile object. One area (referred to as continuously scanned) was EBSD scanned after each strain increment using 32 nA beam current. Another area was scanned prior to straining with 32 nA, at ~5% strain (when the

transformation had just started) and after that only at ~22% of plastic strain (when the material was expected to have a significant amount of martensite). Thus, 4 to 5 scans were omitted.

Figure 19 shows the bcc-phase amount as a function of local strain for different scanning conditions. One can see a strong increase in the bcc-phase amount in the specimen scanned at 8 nA and a very limited increase in bcc-phase in the specimen continuously scanned with 32 nA current.
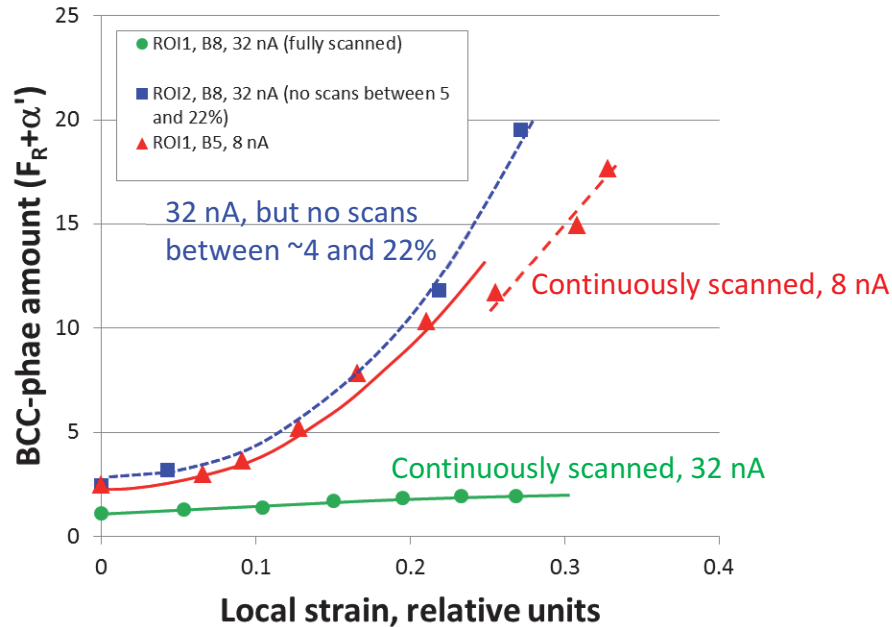
Figure 19. The amount of bcc-phase (both retained ferrite and strain-induced α′-martensite) as a function of the local strain level and EBSD scanning conditions (beam current in nA).

The area scanned using high beam current (32 nA) revealed only retained ferrite and a very small increase in the amount of strain-induced martensite (Figure 18b); the resulting curve is almost horizontal (Figure 19). In contrast, the area, continuously scanned using 8 nA current, demonstrated a pronounced increase in the bcc-phase amount, suggesting intensive phase transformation. Control EDS scans and magnetic measurements for retained ferrite excluded the possibility of mixing specimens. One could speculate that scanning with high beam currents may suppress the phase transformation processes and lead to the misinterpretation of the results.

Interestingly, if no scanning was performed in the strain range between ~5 and ~22%, the beam current value seems to be a neutral or almost neutral factor (Figure 19, blue curve). Phase transformation often develops in a stage-wise manner: appearance (Stage 1) and growth (Stage 2) of the martensite particles and domains. Thus, the results (Figure 19) suggest that beam current value is especially important in the earlier stages of the transformation (small strain range, ~5–10%). Before transformation initiation (<5%) or after formation of the well-developed colonies (>20%), the beam current factor is not so critical in the in situ tests.

The literature on the in-situ EBSD testing of 300-series steels with a particular focus on the phase instability is relatively limited; moreover, just a few papers report the beam current values. The research team was, however, able to find published works reproducing both observations from the present work: successful tracking of the martensitic transformation kinetics and, as believed, suppression of the phase

instability. In situ testing was conducted in [18] for 301 steel, and well-developed phase transformation was observed at ~10% of strain, which agrees with the present work and expectations for the austenitic Fe-Cr-Ni steels with ~7–8% Ni [18].

At the same time, an impressive in situ test reaching large strain levels (~80–90%) was conducted in [17]; tracing of deformation twinning and texture evolution were reported. However, a very small amount of strain-induced α′-phase was reported: <1% at ~55% strain [17], in contrast to [18]. The conclusion could be drawn that the phenomenon connected to high beam current took place.
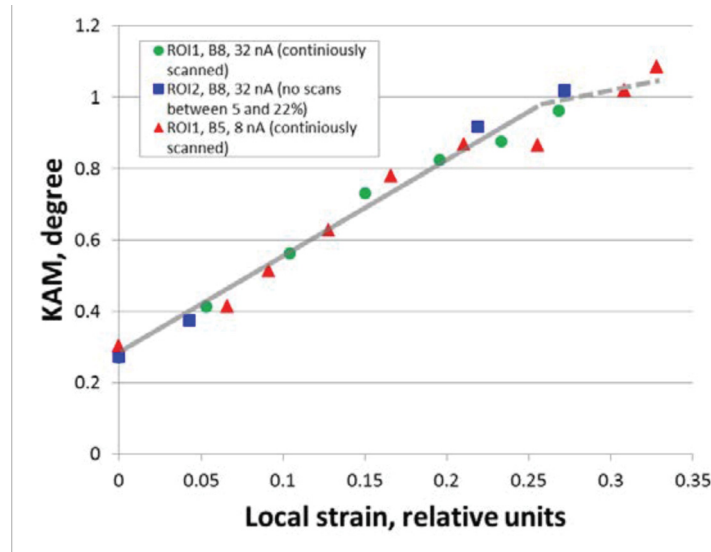
Figure 20. Strain-induced changes in KAM value for the same areas as in Figure 18.

Figure 20 shows the evolution of the KAM value as a function of the local strain for the data sets depicted in Figure 19. One can see that the differences in the strain-induced changes in the KAM value were negligible and that the data points followed the same relationship regardless of the beam current. One could conclude that in the small strain range (0–~0.25 or 25%), there is a close-to-linear relationship between the strain level, KAM, and other EBSD strain metrics [33,34]. Beam current, influencing phase instability during in situ tests, did not affect (or affected insignificantly) the KAM values.

2.4   CONCLUSION

In situ mechanical testing coupled with EBSD analysis was conducted using specimens of two 304L steels, which serve as reference materials for specimens irradiated in nuclear reactors. The results demonstrated that a single specimen could be used to investigate the changes in the EBSD KAM parameter and other EBSD strain metrics. Deformation twins appeared at strain level, comparable to the ex situ experiments. At the same time, as expected, kinetics of martensitic transformation was influenced by the beam current value used during the EBSD scans. Continuous scanning using 32 nA beam current led to the suppression of the phase instability in the near-surface layer, but acceptable results that were comparable to the bulk were obtained using 8 nA beam current. The exact role of the beam current is unclear, but it appears to be neutral regarding the misorientation evolution (i.e., EBSD GROD and KAM behavior) and deformation-induced twinning. While important at room temperature, this issue is thought to disappear at the LWR-relevant temperature. Nevertheless, the potential sensitivity of the acting deformation mechanisms to the in situ test conditions (e.g., beam current or time between the steps) should be considered.

3. IN SITU TENSILE TESTING COUPLED WITH NEUTRON DIFFRACTION ANALYSIS

3.1 INTRODUCTION

Instead of the important advantages of the EBSD approach (e.g., high spatial resolution), neutron diffraction analysis has much better capability to quantify elastic strains and evaluate defect density. EBSD does not allow for nondestructive evaluation of material in the bulk. In contrast, neutron diffraction allows for measuring the undersurface layers and the bulk material. Quantifying elastic strains (and, thus, stresses) is a well-established routine for the neutron diffraction approach. Additionally, diffraction peak broadening provides a way to measure defect density in the crystal lattice. Both methods—in situ SEM-EBSD and in situ neutron diffraction analysis—appear to be complementary with regard to assessment of the radiation damage and strain-induced changes in the structure of irradiated material. Performing in situ neutron diffraction tests and SEM-EBSD-based deformation experiments on the same alloy may be considered a powerful research tool combination.

The literature is very limited literature regarding in situ mechanical testing coupled with neutron diffraction analysis of irradiated austenitic steels. Thus, it was decided to conduct a trial test with a high-dose (~10 dpa or more) specimen. The primary goal was to establish the sensitivity of the diffraction-based approach to the strain-induced changes in the structure with a focus on the small strain area and load levels below the nominal yield stress. To simplify the pilot test, testing was conducted at room temperature only.

3.2 TEST MATERIALS

The materials tested were 10.7 dpa neutron-irradiated M-alloy (304 stainless steel with the addition of 0.3% Ti [11]) and an unirradiated substitute (i.e., reference) alloy of the same composition and fabrication route. The M-alloy was produced in the framework of the CIR program [11] in the early 2000s. The set included more than 12 different alloys based on 304L composition and was alloyed to enhance different material performance metrics [11]. The specimens were irradiated in the BOR-60 fast reactor [12] and used in several projects [5,23,28].

The specimen for the in situ tensile testing reported here was made from a fragment of a tested round compact tension specimen made in M-alloy [11]. The processing route of the original M-alloy was known and included final cold-rolling by 60–70% thickness reduction followed by a final annealing at 950°C for 30 min. Figure 21 shows a typical microstructure of the irradiated M-alloy; it shows relatively small average grain size, about 10 μm, and a pronounced bimodal grain size distribution. Small grains formed specific clusters or bands, and large grains often grouped together. Two phases were identified: (1) austenite, fcc, and (2) delta-ferrite, bcc. Phase identification was confirmed by hand analysis of recorded Kikuchi patterns. The amount of delta-ferrite visible with EBSD was estimated to be ~1–1.5%.
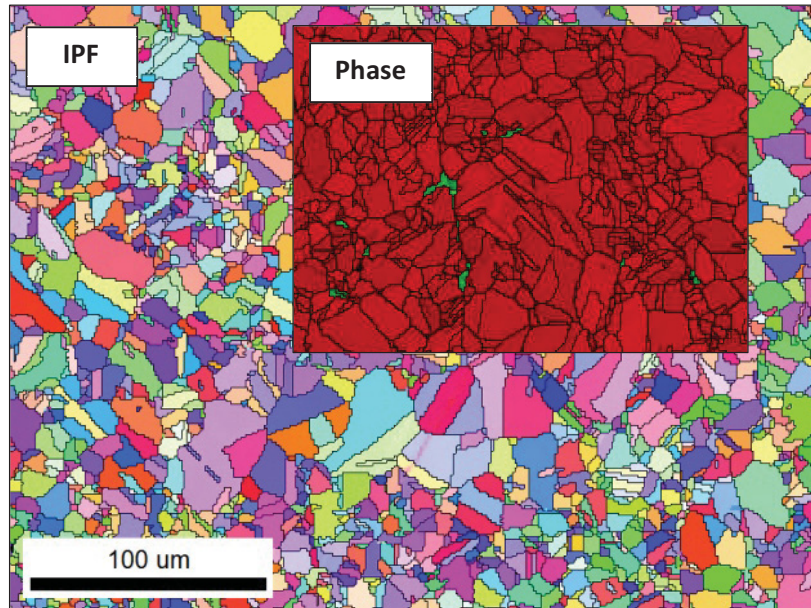
Figure 21. Typical microstructure (EBSD IPF map) of Ti-enriched 304L steel. Inset is the EBSD phase map for the same area (austenite is red, delta-ferrite is green).

As archive M-alloy was not available, a substitute alloy of the same composition was produced through a processing route similar to the one used for the irradiated M-alloy. The final annealing was done at 975°C for 30 min to reproduce grain size. However, it was impossible to reproduce texture, grain morphology, and amount of the retained delta-ferrite.

3.3 SPECIMEN GEOMETRY

A tensile specimen geometry called SNS-T was designed for the test. The nonstandard design ensured that:

- enough material was available from the irradiated M-alloy fragment,

- the activity level of the tensile specimen was acceptable for testing at SNS, and

- necking occurred at the center of the gauge (i.e., in a region fully exposed to the neutron beam). Specimens irradiated at high doses (~10 dpa or more) typically have zero or very limited uniform elongation, and the neck formation can occur anywhere along the gauge.

The SNS-T geometry (Figure 22, left panel) has a relatively short gauge, with gauge dimensions of 3.2 × 1.6 × 1.6 mm with small local thinning in the center. Limited numerical simulations and trial ex situ tests with cold-worked austenitic steel specimens demonstrated that localized deformation develops and necking forms close to the specimen center, under the neutron beam.

The irradiated tensile specimen (Figure 22, right panel) was produced at the ORNL's LAMDA facility via CNC machining. Flat specimen surfaces were mechanically ground using 1200 grid sandpaper to fit the thickness dimensions. Nonirradiated tensile specimens were produced using an EDM.
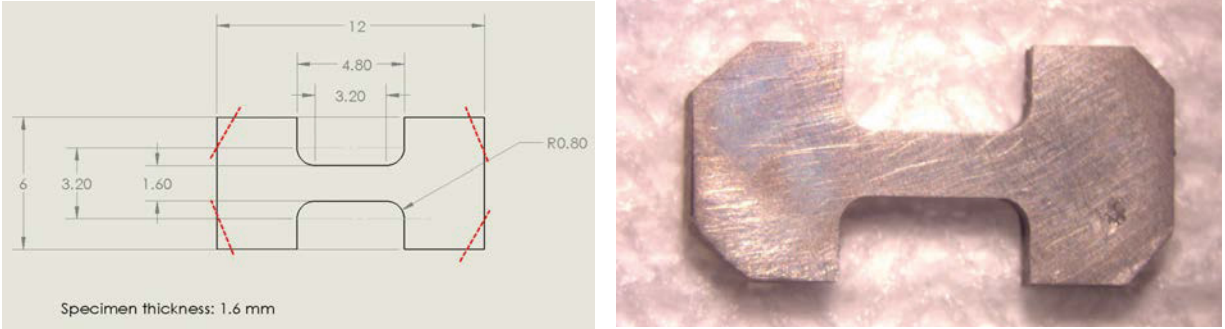
Figure 22. The geometry of tensile specimen for in situ testing at SNS. Dimensions are in millimeters. Small fragments were cut from the specimen heads to allow specimen preparation with the Minimet device.

Grips were designed to accommodate the SNS-T geometry and the SNS setup, which includes having openings for the neutron beam (Figure 23). Since the test materials are mostly fcc phase, grips were fabricated out of bcc-phase material to more easily differentiate between diffraction data due to the grips versus the tensile specimen.
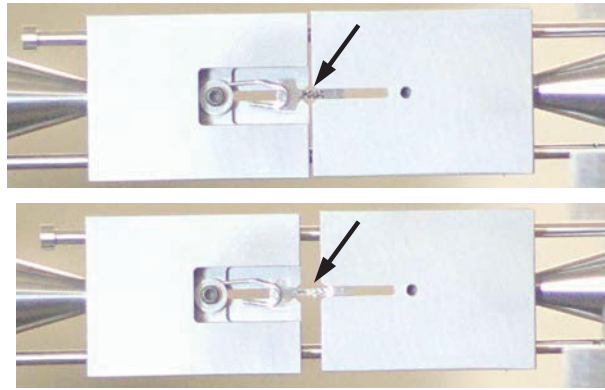
Figure 23. Unirradiated specimen (black arrows) in the grips at 0% (top) and 80% (bottom) engineering strain.

3.4   EXPERIMENTAL SETUP

In situ testing was conducted at the engineering time-of-flight neutron diffractometer VULCAN, described in detail in [35–37]. The high-intensity mode was employed, corresponding to a 0.6–3.4 Å wavelength range. The location of the two detectors [38] allowed for detecting diffraction peaks originating from {hkl} planes with normals aligned with the loading direction or with the normal direction, according to the detector. In the rest of the text, <hkl> grains refer to grains that are aligned such that one of their <hkl> directions is aligned with the loading direction.

One irradiated specimen and one reference specimen were tested in situ while collecting neutron diffraction data. For both specimens, the test was conducted at room temperature at a strain rate of $3 \times 10^{-4} s^{-1}$. The experiment consisted of several steps: #1, loading up to ~90% of the yield stress and unloading down to ~100 MPa to catch the structure evolution below the formal yield stress limit, #2, straining at small strain level (~1–2% of plastic strain) to investigate processes in the small strain area, and, #3, exploring large (~10–20%) strain levels. Straining was done in load control mode for step 1, and in displacement control mode for steps 2 and 3. Straining was stopped every 50 MPa or 0.1% strain to collect diffraction data for 10 min. To avoid deformation creep when stopping the straining, the load was

relaxed by a few percentage points before collecting diffraction data. From 1% strain and higher, the strain increment was increased to 1%.

Images of the strained specimens were recorded to estimate true stress/strain through digital image correlation. The engineering and true stress strain curves for both tests are shown in Figure 24.
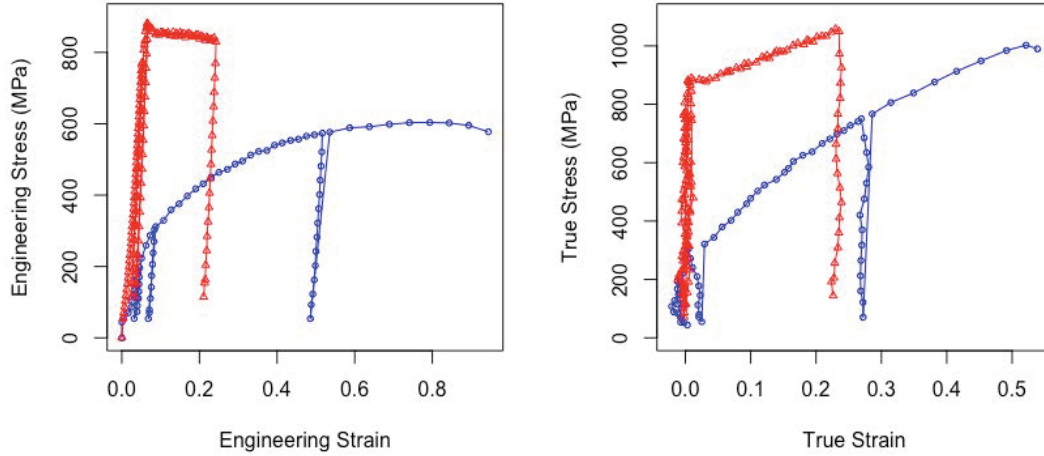
Figure 24. In situ stress strain curves of the unirradiated (blue circles) and irradiated (red triangles) test specimens in engineering (left) and true (right) stress and strain.

3.5   ANALYSIS METHOD

Data were analyzed with software VDRIVE [39] using the single peak fitting function based on GSAS TOF profile function 3 [40]. It relies in particular on the pseudo-Voigt approximation [41], which considers a Gaussian component and a Lorentzian component to the peak broadening. The outputs of single peak fitting are:

- the peak position d_{hkl}, which corresponds to the interplanar spacing of the diffraction planes and is expressed in Å,

- the peak intensity I_{hkl}, and

- the peak broadening hereby characterized by the full widths at half maximum of the peak's Gaussian component Γ_{hkl}.

The lattice strain per {hkl} planes is given by $\varepsilon_{hkl} = \frac{d_{hkl} - d_{hkl}^0}{d_{hkl}^0}$, with d_{hkl} the instantaneous peak position and d_{hkl}^0 the peak position at 0% strain. The texture is evaluated with the texture factor $p_{hkl} = \frac{I_{hkl}/I_{hkl}^P}{\sum_{i=1}^8 w_{hkl} \times I_{hkl}/I_{hkl}^P}$, with I_{hkl}^P the measured intensity for the specimen before straining, which is approximated to a powder untextured sample, and w_{hkl} the weighting factor accounting for the inhomogeneous contribution of <hkl> grains to the total diffracted intensity, as detailed in [38]. The quasi-Monte Carlo reconstruction of the Inverse Pole Figure (IPF) is described in [38]. In unirradiated crystals, the broadening of the Gaussian component to the peak is due to dislocations introduced by plastic deformation. The increase in broadening can be used to evaluate the increase in dislocation density, for example, using Wilkens analytical model [42]. In irradiated crystals, the broadening is also

due to preexisting radiation defects. The results below show only the absolute value of Γ_{hkl} for both specimens. Further analysis will attempt to characterize the evolution of preexisting radiation defects and dislocations in the irradiated alloy.

3.6   EXPERIMENTAL RESULTS

3.6.1   Lattice Strain Evolution

Figure 25 shows the evolution of lattice strains with strain and stress for three (hkl) reflections in the reference and irradiated specimens up to about 25% strain. The elastic anisotropy of the material is captured during the elastic loading: The elastic strain evolution and yield stress per (hkl) grain family can be estimated. In the plastic regime, the evolution of lattice strain is controlled by dislocation activity. An increase in (hkl) lattice strain in the plastic regime is associated with work hardening in the corresponding grain family. Interestingly, some grains (close to <110> direction) undergo work softening in the irradiated alloy.
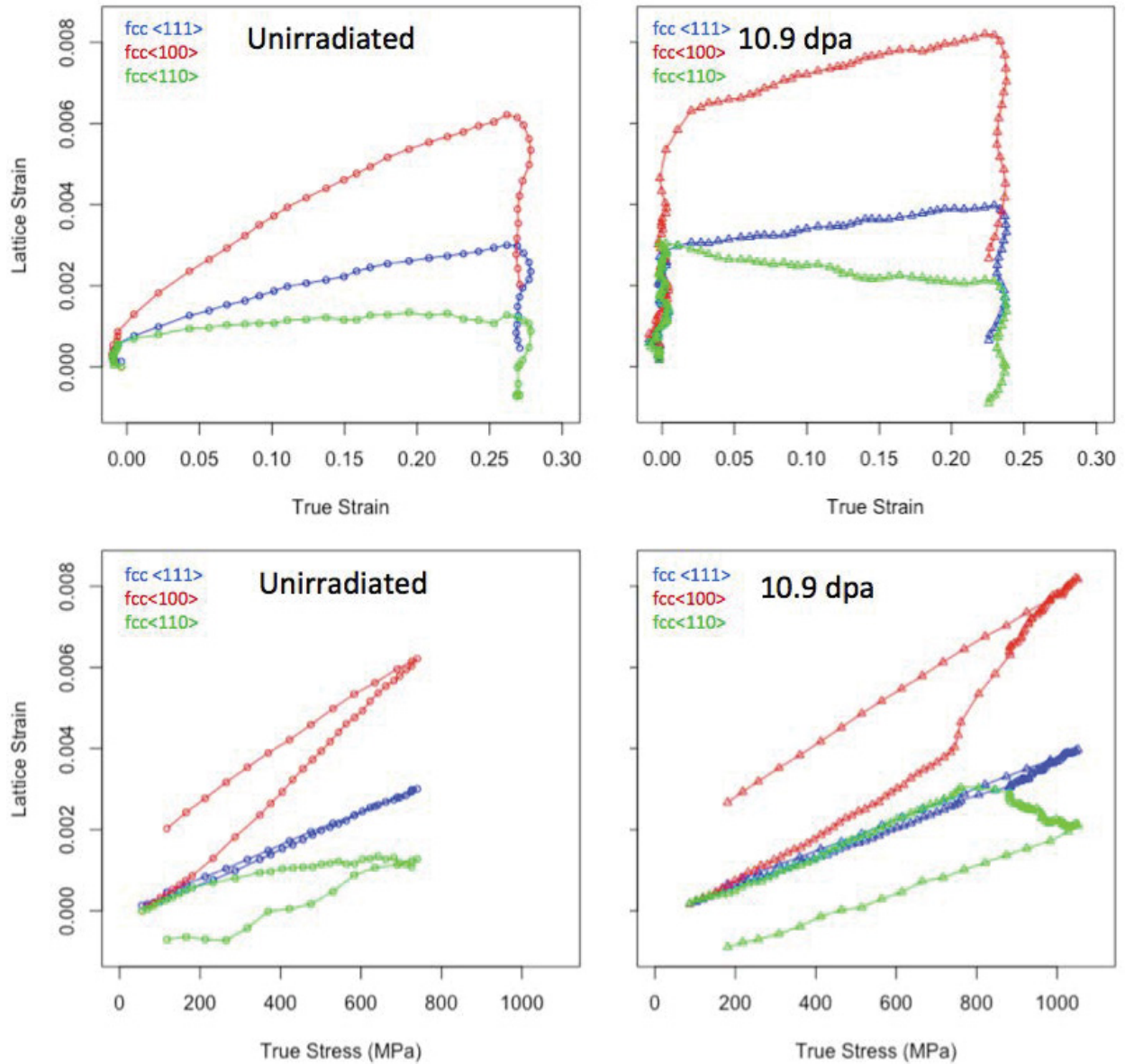
Figure 25. Evolution of lattice strain with macroscopic true strain (top row) and true stress (bottom row) for the reference sample (left column) and the irradiated sample (right column) for three (hkl) reflections.

3.6.2   Texture Evolution

Figure 26 shows the evolution of texture parameters for the reference and irradiated specimens. Typical texturing is observed in both cases: rotation of grains towards the <111> and <100> directions and away from the <110> direction. The evolutions of the <100> and <110> texture parameters look similar. The <111> texture parameter increases faster in the unirradiated specimen. Note that in the irradiated case, necking occurs right after yield and the straining from 0 to 25% true strain is a phase of prolonged necking—in the unirradiated case, the straining from 0 to 25% true strain happens prior to necking (which occurs at about 40%).
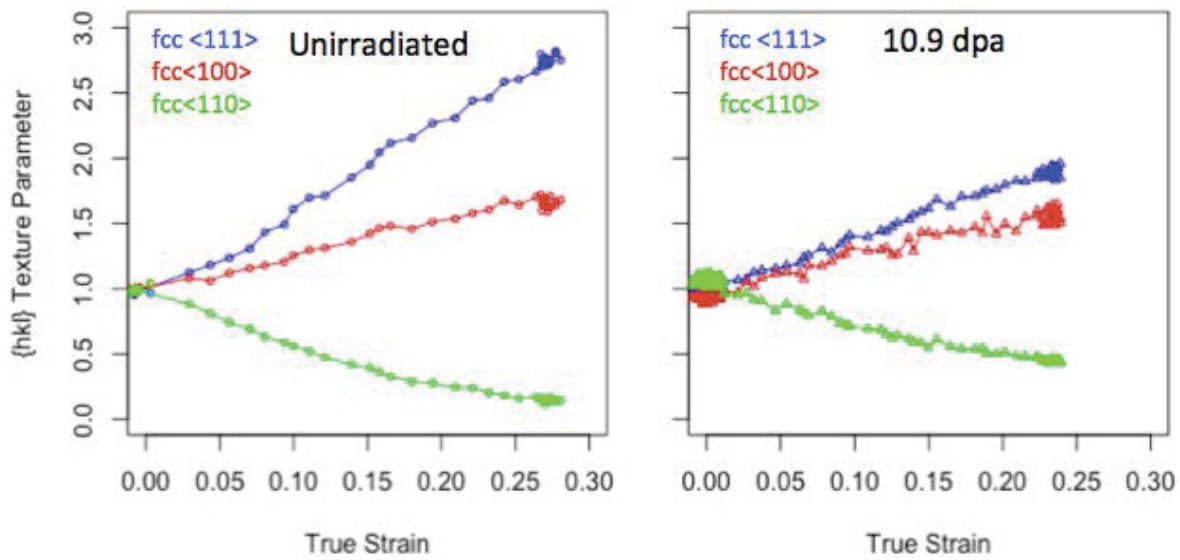
Figure 26. Evolution of texture parameters with macroscopic true strain for the reference sample (left) and the irradiated sample (right) for three (hkl) reflections.

3.6.3   Peak Broadening Evolution

The evolution of the full width at half maximum of the peak's Gaussian component Γ_{hkl} for the reference and irradiated specimens is shown in Figure 27. Note that the initial broadening of the irradiated specimens is larger, which is likely due to the presence of radiation-induced defects. Further analysis will use the broadening to determine the evolution of dislocations and radiation defects.
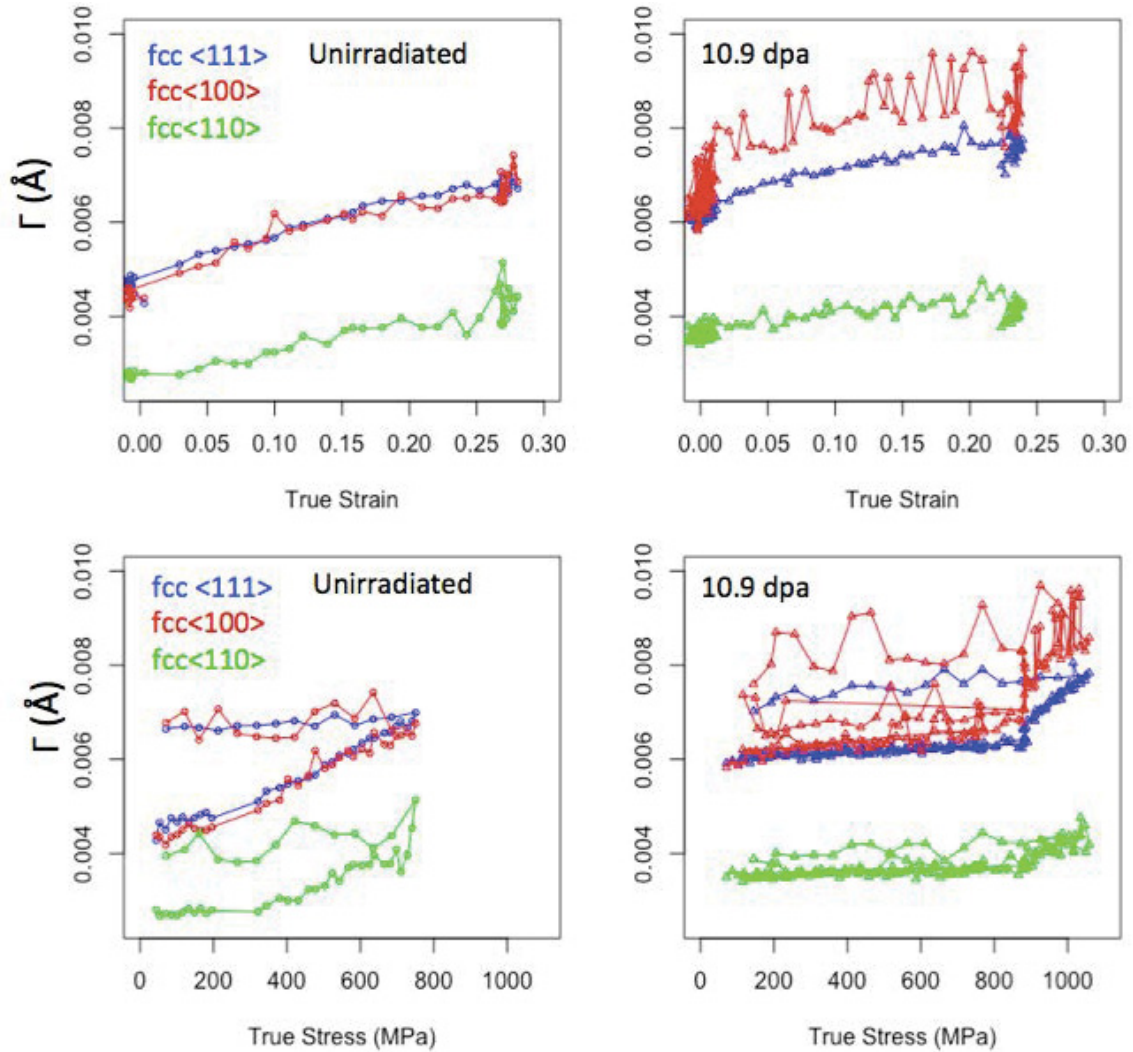
Figure 27. Evolution of peak broadening with macroscopic true strain (top) and true stress (bottom) for the reference sample (left) and the irradiated sample (right) for three (hkl) reflections. The broadening is evaluated as the full width at half maximum of the peak's Gaussian component (Γ) and is expressed in Å.

3.7   CONCLUSION

In the present work, the first tensile test with the irradiated specimen was conducted at the SNS VULCAN facility, yielding new and important results regarding strain/stress partitioning between grains of different families, measurement of retained stresses, diffraction peak broadening, and defect density evolution in situ. If funding permits, the same irradiated material will be tested using SEM-EBSD approach.

4.   IN SITU SEM-EBSD TENSILE TESTING

4.1   MOTIVATION FOR SEM-EBSD IN SITU TENSILE TESTING

Neutron irradiation, leading to the formation of radiation defects, influences most of the strain-induced processes and stimulates deformation localization. In the neutron-irradiated austenitic steels, multiple fine slip lines typical for nonirradiated materials are replaced with coarse defect-free dislocation channels. Interacting with grain boundaries and second phase domains, the defect-free channels lead to high local

stress and strain levels and phenomena not usually seen in the nonirradiated steels with multiple fine slip lines. A vast literature exists on the deformation localization in neutron irradiated materials; however, the majority of results are based on the posttest structure characterization. Postmortem testing, while yielding important and valuable information, provides limited data on the kinetics of the process.

It is well known that the local structure (or local grain configuration) strongly influences a material's performance. EBSD is a suitable modern tool providing local crystallographic information with resolution up to 100 nm or even better and allowing for connection of local material structure and different material performance metrics.

As discussed previously, coupling EBSD with in situ mechanical testing provides numerous important benefits. For example, the same specimen may yield information for a wide range of stress and strain levels. Tracking the same area through different strains may reveal stages and important details of the strain-induced phenomena. Rich literature is available on the SEM-EBSD in situ testing of nonirradiated materials, and this area has experienced impressive progress over the last few years. However, very limited, if any, work was performed on the neutron-irradiated steels and alloys.

It is believed that SEM-EBSD in situ tensile testing will be a key approach for investigating texture evolution and grain rotation effects in neutron-irradiated materials, dislocation channel–grain boundary interactions, and local misorientation evolution and for evaluating EBSD strain metrics like KAM and GROD for irradiated polycrystals. The present section describes the results of a pilot in-situ tensile test with irradiated austenitic steel.

4.2   INVESTIGATED MATERIAL, SPECIMEN GEOMETRY, AND PREPARATION

A nuclear-grade, high-purity AISI 304 austenitic stainless steel irradiated in LWR at 5.9 dpa was selected for this study. This material (see Table 2 for composition) was left over from a previous project and had an annealed austenitic structure (Figure 28) and an average grain size of ~65 μm. The material was provided by Studsvik Nuclear AB and was cut from a control rod made of Type 304L steel produced by Vereinigte Edelstahlwerke AG (Böhler), Austria. The control rod was in operation in the Barsebäck 1 boiling water reactor in Sweden. The neutron flux was calculated by Barsebäck using the in-core fuel management code POLCA, and the calculated damage dose was 5.9 dpa.

Table 2. Composition (wt%), grain size, and expected deformation mechanisms for the 5.9-dpa irradiated steel

Internal material code	Description	Fe	C	Mn	Si	Cr	Ni	Mo	N	Grain size (μm)	Expected deformation mechanisms
SW2	Nuclear-grade, high-Ni 304L steel	Bal.	0.025	1.09	0.30	18.35	10.57	–	0.024	55–60	Dislocation slipping, twinning

Due to the relatively high Ni content (10.45%), the material was expected to have limited phase transformation intensity with pronounced deformation twinning. Metallography analysis showed large, equiaxial austenitic grains and very low density of nonmetallic inclusions. Magnetic measurements showed the presence of a small amount of magnetic phase, ~0.15–0.2%, presumably, delta-ferrite.
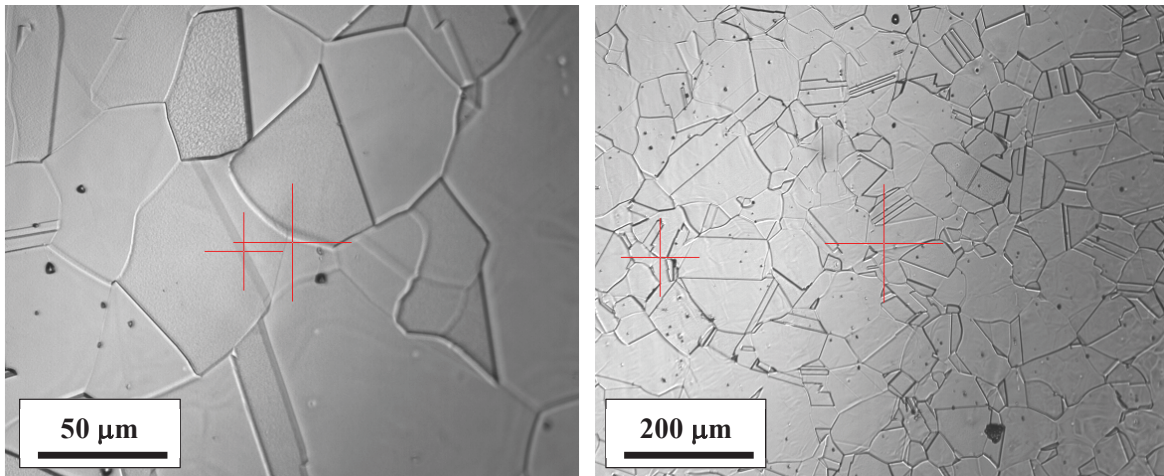
Figure 28. The structure of the neutron-irradiated 304L steel. The sample was prepared via mechanical grinding, electropolishing, and etching with 10% oxalic acid).

Miniature specimens of SS-Tiny geometry (Figure 9) were produced at LAMDA using CNC machining, as described above. After CNC machining, standard surface preparation (i.e., mechanical grinding down to 3-µm diamond sandpaper with electropolishing as the final step) was conducted to provide a clean, defect-free surface. Figure 29 illustrates the surface quality; after electropolishing, the surface quality was free of defects and cold-work. Few inclusions were visible at the surface. Fine slip lines (i.e., defect-free channels in the irradiated steel) introduced by microhardness indentation were clearly visible with an optic microscope.
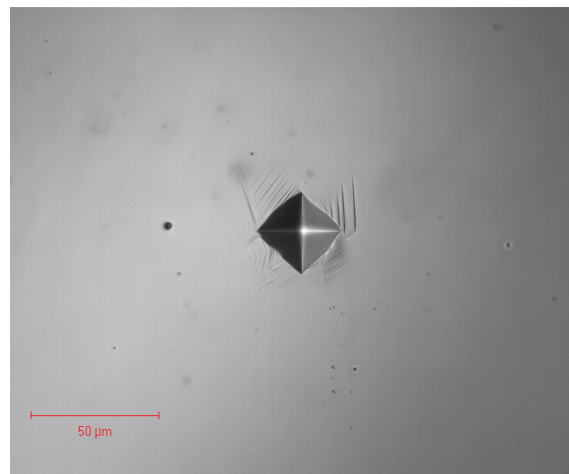
Figure 29. The surface of the specimens after final preparation step (electropolishing). Microhardness indentation surrounded by slip lines illustrates the surface quality and absence of any sediments or film at the surface.

4.3   TENSILE CURVES FOR EX SITU AND IN SITU TESTS

To provide the basic mechanical properties and load and strain levels for the following in situ test, one miniature specimen was tested ex situ, in the air; the strain rate was $10^{-3}s^{-1}$. The ex situ deformation experiment was interrupted slightly before the fracture; however, a pronounced neck formed at the

specimen gauge. It appears the total elongation value is slightly underestimated, but this should not be an issue for the present work purposes.
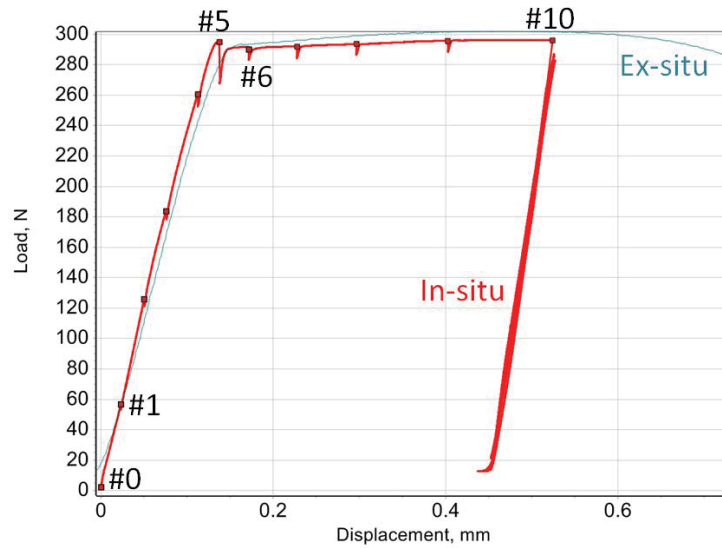
Figure 30. Tensile curves obtained for the ex situ (thin blue line) and in situ (thick red line) tensile tests. The labels show the load and displacement values for the EBSD scans performed at the selected locations.

The tensile curves for both tests are shown in Figure 30; both specimens demonstrated comparable yield stress (Table 3) and similar mechanical behavior. There was a very weak difference between the specimens; the observed variations may be explained by the material's natural inhomogeneity. The small irradiated plates used to produce the tensile specimens were nominally identical but came from slightly different locations along the control rod blade. Thus, small differences could be expected.

Table 3. Mechanical properties of tested irradiated specimens

Type	Yield stress, MPa	Ultimate stress, MPa	Uniform elongation, %	Total elongation, %
Ex situ at RT	795.6	862.6	17.4	29.56
In situ at RT	766.2	871.3	~19	n/d
As-irradiated, tested at 288°C*	672	672	0.03	11.2

*Data were provided by the irradiated material vendor. RT refers to room temperature, 20°C

4.4   DESCRIPTION OF IN SITU TEST PROCEDURE

Any SEM-EBSD in situ test is a compromise between the number of steps, dimensions of the analyzed (or scanned) area, and resolution (i.e., step size or pitch). Since EBSD scanning is time consuming and limited with regard to time on the instrument, number of scans and deformation steps were limited. It was decided the test would focus on the small plastic strain area so that possible strain-induced phenomena could be explored in detail. Two ROIs were supposed to provide information on the small plastic strain level. Additionally, detailed EBSD scans of the elastic loading region were conducted to explore the early channel formation and evolution, and one area was designated to explore the large strain area.

Thus, four ROIs (shown as R on figures) were identified at the tensile sample surface (Figure 31). The ROIs were distributed along the gauge to maximize the chance to catch the maximum strain area inside the neck. The particular locations were selected to avoid inclusions or other surface peculiarities or damaged spots. Preliminary EBSD scanning with coarse step size was performed to ensure each ROI contained at least several (10–20) grains of different orientation.

After analyzing the irradiated material behavior (Figure 30), the load values of ~0.25, 0.5, 0.75, and 1 of yield stress value were chosen to explore the elastic strain region. The last scan performed at ~1 yield stress corresponded to the nominal strain level of ~0.2% or (~0.002) in the engineering strain terms.

After that two steps were performed with nominal ~0.5 and ~2% strain increment. Intense surface roughness and surface relief were expected to develop, creating shadows and making the EBSD scanning too complicated for some areas. However, several more steps were performed with a 2–4% increment; the experiment was stopped after the nominal ultimate stress point was reached. The final nominal plastic strain level was ~19–20%. Table 4 summarizes the experiment loading and deformation steps. Reference EBSD data were obtained for all ROIs, but not all ROIs were scanned at every strain or load step.
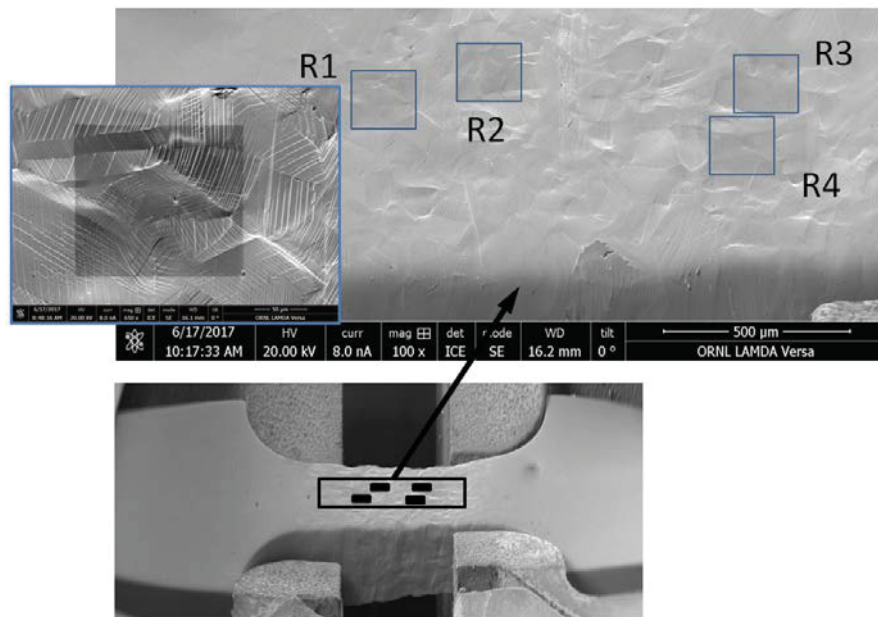
Figure 31. ROIs identified at the specimen gauge. Note the images show a deformed specimen. All images are 70°-tilted; small magnification for the bottom image shows the whole tensile specimen but leads to significant aberration and distortion.

Table 4. Summary of the deformation steps performed for different regions of interest

Step no.	Fraction of yield stress	Global plastic strain*	Engineering global stress (MPa)**	R1	R2	R3	R4
0 (reference)	0	0	7.1***	•	•	•	•
1	~0.216	0	166.8				•
2	~0.482	0	370.0				•
3	~0.705	0	540.9				•
4	~1.0	0.002	766.2				•
5		0.007	867.9		•		•
6		0.025	853.5	•		•	•
7		0.053	859.1		•		•
8		0.087	864.1	•		•	
9		0.137	870.3			•	
10		0.2	871.2			•	

*Engineering strain definition is used; strain value is presented in the dimensionless units.
**External load value immediately divided by the sample initial cross section.
***Some minimal load (~2.4 N) was applied to keep the specimen alignment and minimize any possible shift during specimen loading, vacuum chamber pumping, and stage movements inside the chamber.

4.5 LOCAL STRAIN EVALUATION

Austenitic steels irradiated at damage doses of several dpa or more are prone to macroscopic deformation localization (i.e., necking). Often the neck forms immediately after the yield stress is reached. Thus, during the experiment, local strain values at the specimen surface may be different from an externally applied nominal strain (i.e., global strain). The difference can be fairly severe, leading to scattering in the results and complicating data analysis.

To measure the local strain level, the same specific points (e.g., inclusions in the SEM images or triple junction points in EBSD maps) were used as fiducial marks and tracked through the data sets for all strain levels, as discussed in Section 2.2. The distance between the points, treated as a virtual strain gauge, was used to calculate the local strain levels [31]. Typically, 5 to 7 gauges were evaluated and averaged for every ROI.

The virtual strain gauge reports the strain value in the tensile axis direction (i.e., X-strain) allowing for calculation of engineering strain. Note that this approach is somewhat limited because a complex stress state is expected for the neck and inside grains; to fully characterize the complex stress state and complex strains, one also needs strains in the transverse (Y) direction and shear strains. Potentially, these strain components will allow for calculation of von Mises strain or another metric, better describing the strain processes. However, employing von Mises strain requires more methodical work. At this time, it is believed that the engineering strain definition is sufficient and inaccuracy, if any, is the same for all ROIs and deformation steps.
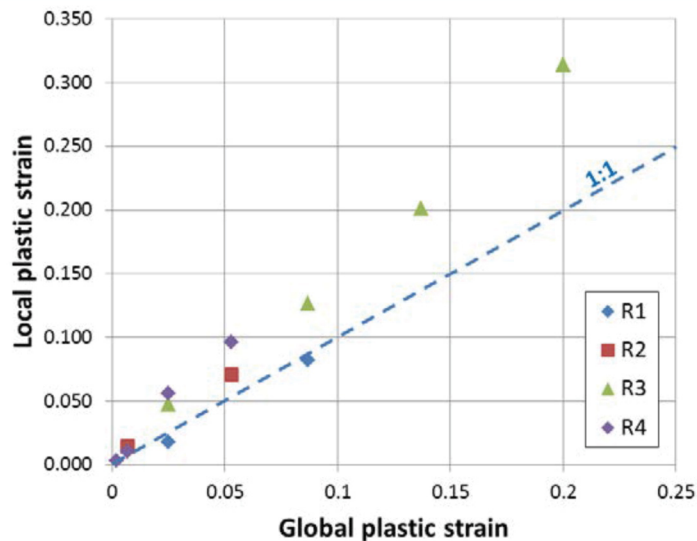
**Figure 32. The relationship between the global plastic strain
calculated from the tensile curve and local plastic strain
measured for the studied ROIs (R1–R4).**

Figure 32 shows the relationship between global plastic strain calculated from the tensile curve and local strains for each ROIs at every deformation step. One can see that, only for R1, the ratio between global and local strains is close to 1, and, most likely, this result comes just by chance. R1 is located at the neck edge, and for this location the local strains, in some strain range, will be close to the global strain value. For other ROIs, located close to the specimen center, the local strain values are always larger compared to the global strains and the difference may reach a factor of ~2. The employed specimen geometry has a relatively short gauge to minimize the area to be scanned prior the test; for this geometry, the neck occupies most of the gauge portion. The gauge fraction not involved in straining and the difference between local and global strains will be larger for the longer specimen, like SS-J or SS-3, where the neck will consume an only small portion of the gauge.

If the specimen of interest experiences nonuniform deformation, using global strain value for multiple ROIs may lead to confusing, misleading results. EBSD strain metrics below are plotted and discussed as a function of the local plastic strain for the given ROI at the given strain step.

4.6   MATERIAL STRUCTURE PRIOR THE TEST

As mentioned above, metallography analysis revealed mostly annealed austenitic structure (Figure 28); no signs of cold work or pronounced deformation bands were revealed by etching. EBSD analysis prior to the test also revealed virtually strain-free austenitic grains (Figure 33). The in-grain misorientation level (i.e., GROD) for all ROIs did not exceed 3–3.5°.

This value is typical for annealed austenite; some "retained" misorientation is likely caused by sparse dislocation population and/or small thermal strains during quenching or cooling. Diffuse areas with smoothly changing misorientation gradients sometimes exist near grain boundaries (Figure 33, label #2). At the same time, several specific elements—relatively sharp in-grain changes in the GROD value (labels #1 and #3)—suggest postirradiation deformation. The features are sharp compared to diffuse prior-irradiation slip lines. One could speculate that the material experienced some insignificant overloading and damage while in service or during object extraction and cutting. Because the material was part of the control rod, occasional mechanical loading and stresses were expected to occur.
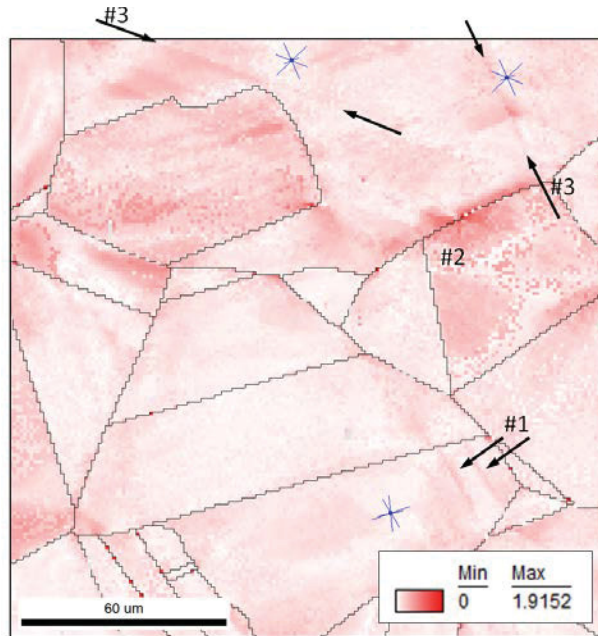
Figure 33. GROD map for R4 prior the test. Label #1 highlights weak in-grain traces of slip lines. Label #2 shows the area with increased local misorientation along the grain boundary. Labels #3 paired with black arrows depicts several multiple weak slip lines.

4.7 SPECIFIC EVENTS AND SURFACE TOPOLOGY EVOLUTION IN THE YIELD STRESS VICINITY DURING IN SITU TENSILE TEST

As mentioned above, neutron irradiation leads to changes in the plasticity mechanisms and multiple deformation localization phenomena. Deformation localization depends on the dose, irradiation conditions, alloy composition, and other factors. Starting at ~few dpa, multiple slip lines in austenitic steels are being replaced by coarse defect-free channels visible at the surface as coarse steps. Defect-free channel formation depends on loading conditions; usually, initial channels appear below the engineering yield stress limit.
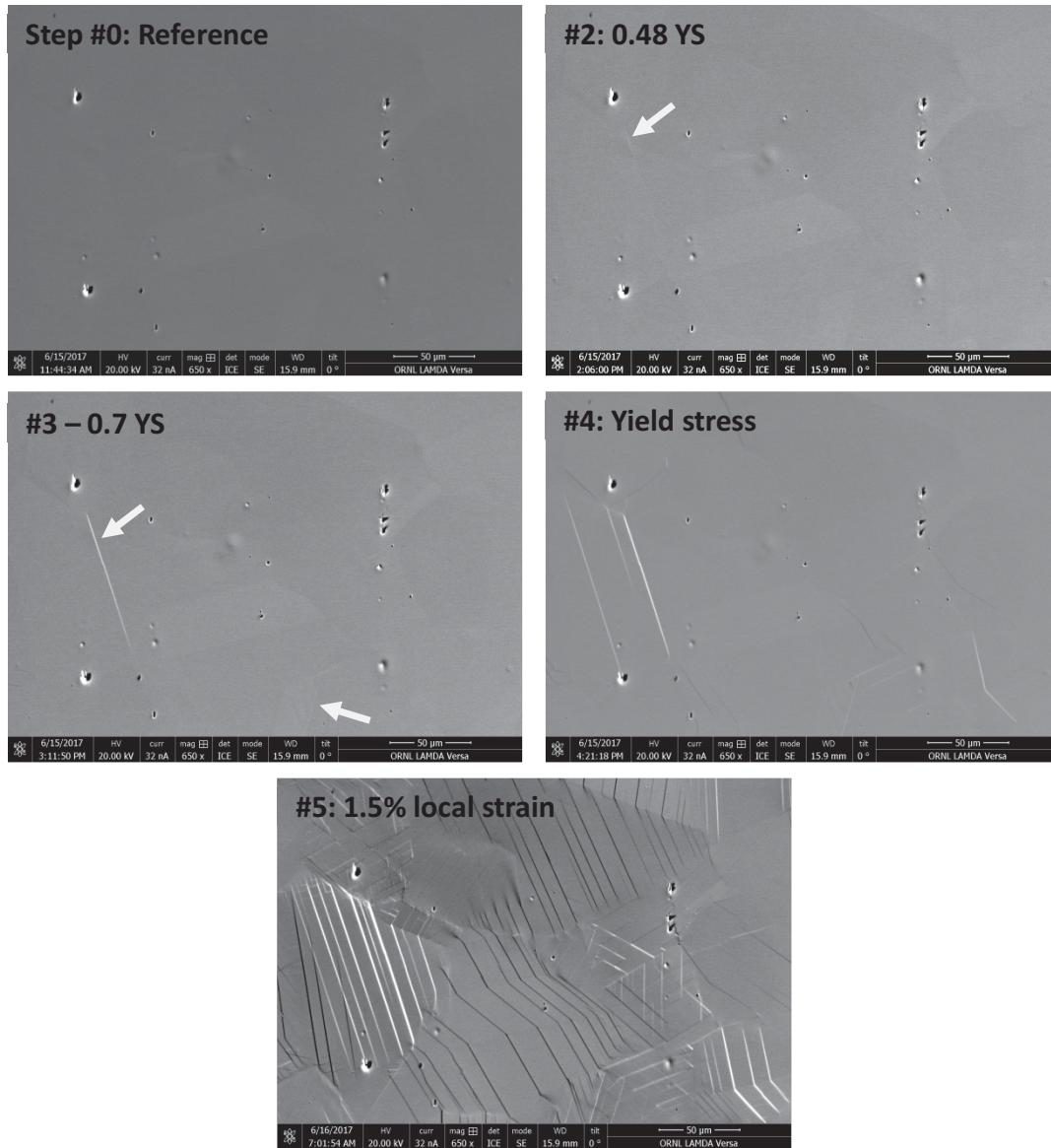
Figure 34. Surface topology evolution for the R4. Arrows indicate the defect-free dislocation channels; the first channel became evident at 0.48 yield stress (step #2).

Figure 34 shows the typical evolution of the specimen surface at small loads (below or at the engineering yield stress). For R4, the first dislocation channel became evident at ~0.48 yield stress (i.e., at about half of the yield stress). At ~0.7 yield stress, this channel moved across the grain and stopped at the grain boundary.

When the engineering yield stress limit was reached (step #4), several channels per grain existed in the field of view; in most grains, only one slip plane was active at this moment. This statement is true for the bulk grain, far from grain boundaries; at the channel–grain boundary interaction point, one may find multiple operational slip planes. Entering the small plastic strain area (step #5) led to the fast increase in the channel density; between one and three active slip planes were operational in each grain.

Figure 35 shows several typical events occurred in the ROI during loading at the yield stress level. Thus, event #1 was an interaction of the dislocation channel with the random high-angle grain boundary

(RHAB); the corresponding EBSD GROD map reveals an increased local misorientation level at this location. Most likely, the increase in GROD parameter was caused by local plastic strain from the high stress level at the channel–grain boundary interaction point. At this step, the channel did not penetrate the grain boundary, and the neighboring grain demonstrates no increase in the local GROD value.
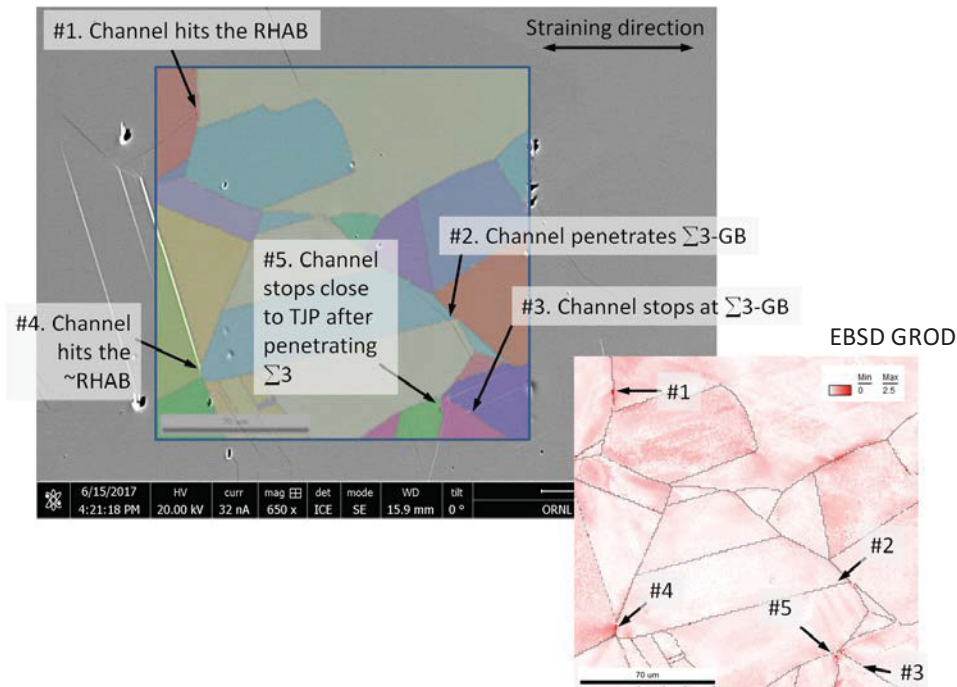
Figure 35. Typical events observed in R4 at step #4 (yield stress vicinity). The plot shows the superposition of SEM image and EBSD IPF map; the insertion at the bottom left demonstrates the corresponding GROD map.

Events #2 and #3 (Figure 35) show the interaction of the dislocation channel with $\Sigma 3$ grain boundary (twin boundary); in this case, channel–grain boundary interaction did not lead to the formation of a high local strain area, in contrast to event #1. Event #4 is a very specific case: The channel propagated along the $\Sigma 3$ grain boundary and finally reached the RHAB. The local increase in the misorientation value is evident in the GROD map. Event #5 is caused by the channel that penetrated the $\Sigma 3$ grain boundary earlier; most likely due to the nonfavorable orientation of slip planes in the target grain no penetration occurred, and a strain localization area started to develop.

Figure 36 illustrates an interesting phenomenon that can be observed and analyzed using in situ testing—dislocation channel self-organization. The appearance of dislocation channels within the grain is not random; the position of the new channel is often controlled by previous, already existing channels. For example, at a small strain level, the grain has two "parent" channels, and next a "child" channel will often form close to the middle or one-third of the distance between the existing channels (Figure 36, left panel). The ratios (1:1 or 1:2) are not perfect and may vary slightly, as illustrated in Figure 36 (right panel). This phenomenon was explored by the research team earlier using an optic microscope and bend-test approach [28]; current work provides more evidence and, if necessary, may provide more statistics. As discussed, dislocation channels self-organization is caused, most likely, by back stress from the dislocation pileups; in the first iteration, the minimum of back stress can be expected in the middle of the two existing channels.
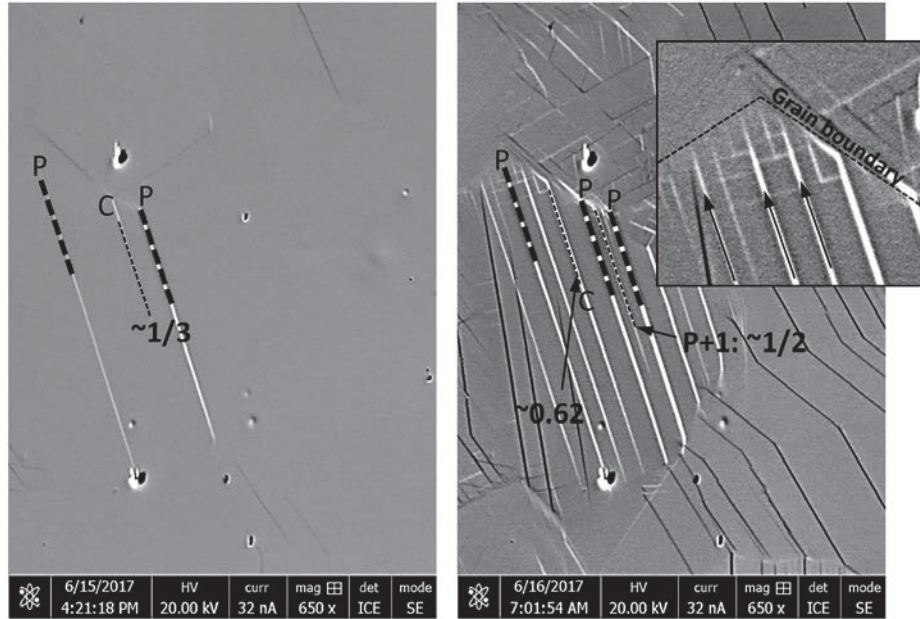
Figure 36. Dislocation channel self-organization during deformation. (Left) Next generation channel (C) forms at ~1/3 between the parent (P) channels. (Right) Next generation channels (C and P+1) form at ~1/2 or ~1/3 (~0.62) between the parent (P) channels. The insertion (an enlarged portion of the image) shows the channel branching near the grain boundary with striking 1/2 and 1/3 ratios.
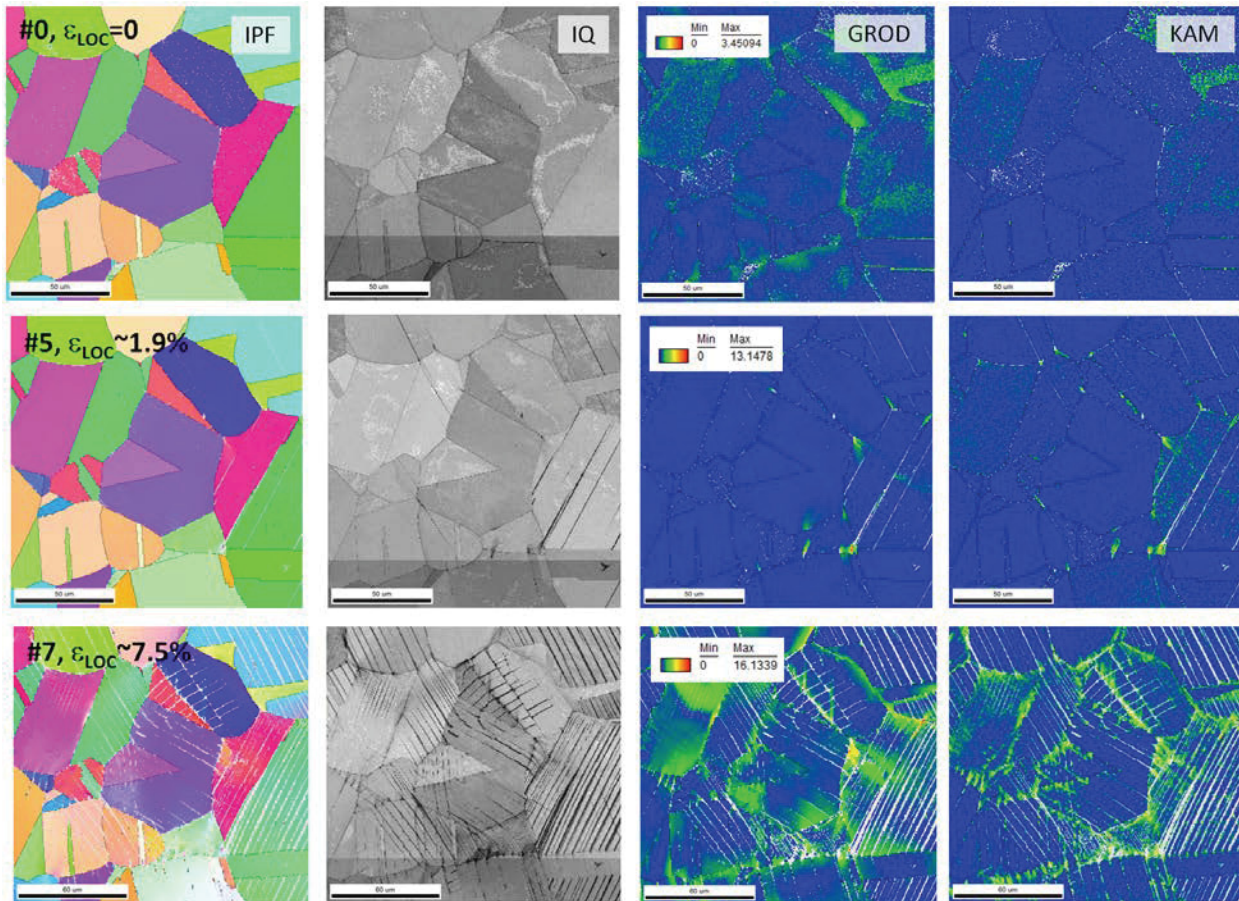
4.8   TYPICAL EBSD DATA SET ANALYSIS

The exact way in which EBSD data are processed, filtered, and analyzed depends on the purposes of a particular project. Usually, the EBSD data set includes an IPF map (colored in the tensile or normal direction) to describe number and orientation of the grains in the ROI, an IQ map to illustrate the pattern and EBSD data quality, and a small number of selected EBSD strain metrics to evaluate strain-induced changes in the structure. In the present work, GROD and KAM parameters were selected as the most typical ones used in the literature. GROD is the most common grain-based approach to describe strain, whereas KAM is a widely used kernel-based strain metric.

Figure 37 demonstrates a typical EBSD data set for a typical ROI; the data set explores a moderate strain area, up to ~7.5% of local strain. The reference data maps taken at zero strain level (step #0) shows deformation-free austenite with low in-grain misorientation (i.e., GROD) below ~3.5°. The reference GROD map shows smooth changes across the grain, most likely caused by dislocations that survived annealing or were generated by thermal stresses during the thermo-treatment. The GROD values for most grains are below 1–1.5°. No specific details may be observed in the reference KAM map, which contains a limited amount of "salt and pepper" noise caused by a generic EBSD error (less than ±0.5°) in the lattice orientation measurement.

As strain level increased to ~1.9%, multiple high-misorientation areas became visible in the GROD and KAM maps (Figure 37, middle row). The local increase in the GROD values reached ~13°; small subareas (typically 1–5 μm) inside grains experienced very high localized plastic strains. Such areas were observed earlier and termed hot spots [5]; at a small strain level the hot spots were not observed in the nonirradiated steel of the same composition. As an ultimate case, local misorientation as high as ~23° after strain and as low as ~0.8% was found and analyzed in detail in [5] after scanning an area of several square millimeters on the 4.4-dpa irradiated specimen.

Here, statistical analyses of these events leads to the conclusion that hot spots always form at grain boundaries or triple junction points. One could speculate that hot spot formation is a relaxation event occurring at the peak stress area near triple junctions or at channel–grain boundary interaction points.

Figure 37. Typical EBSD data set obtained during in situ test: (left to right) IPF, IQ, GROD, and KAM maps.

Once the relaxation has occurred, the hot spot is "exhausted" and not able to generate the same event (e.g., sudden jump in the local misorientation) again. Thus, further increase in the strain level to 7.9% (Figure 37, bottom row) does not necessarily lead to a proportional increase in the misorientation level. Plastic strain increased at a factor of 4, from ~1.9 to 7.5%, but maximum GROD parameter experienced a modest growth from ~13 to ~16°. The hot spots formed earlier also demonstrated relatively small changes; often their maximum GROD values remained the same or increased just slightly. New hot spots emerged along grain boundaries.

The largest GROD values are typically observed at grain boundaries, whereas increased KAM values may be seen at grain boundaries, as well at the intersection of channels (slip lines) within the grain. The space between channels usually has KAM values close to the nondeformed material (i.e., remains practically undeformed).

4.9   STRAIN-INDUCED CHANGES IN THE GROD PARAMETER

Strain-induced changes can be described using an EBSD strain metric averaged across the ROI, or using a maximum observed value. Since GROD is the grain-based approach, this parameter can reveal the

location with the largest change and, thus, strain. For the purposes of the present work, it is reasonable to explore the maximum change in GROD (i.e., to use the maximum GROD value for the selected ROI).
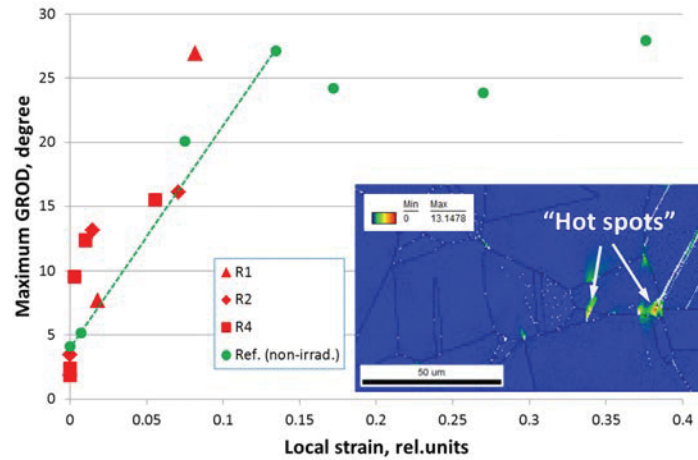

Figure 38. Maximum GROD value observed within the EBSD scan as a function of the local plastic strain level.

Obviously, the initial or reference GROD values strongly depend on the material history and for annealed austenitic steel usually do not exceed 2–4° (Figure 38). As strain level increased in the present work, GROD increased as well due to the dislocation accumulation in the grain body and near grain boundaries. For nonirradiated steel, the maximum GROD value, observed in some ROIs, increased linearly with strain level and saturated after $\varepsilon\sim0.15$. A sharp break at this strain level was caused by grain fragmentation and high-angle boundary formation within grains. Small strains corresponded to the relatively smooth changes in the maximum GROD. Thus, maximum GROD values observed within a scanned area may serve as a rough indicator of strain level.

In contrast, irradiated material shows very fast and unpredictable growth in the GROD in the small strain area due to the formation of deformation hot spots (Figure 38). The appearance and strain amplitude within hot spots were fairly random; thus, the resulting points in the plot formed a specific cloud above the reference specimen curve. Furthermore, the presence of the high GROD locations (hot spots) in the irradiated material structure testifies to the fact that the material experienced plastic strain; however, strain level cannot be estimated using only this parameter.

4.10 STRAIN-INDUCED EVOLUTION OF THE KAM VALUE

KAM is one of the most common strain metrics employed by researchers [33,34]. If obtained, reference or calibration KAM(ε) curves may be used to quantify damage accumulated during deformation or while in service [19,33,34]. In most cases, KAM increases linearly with strain level and tends to saturate after some threshold strain.
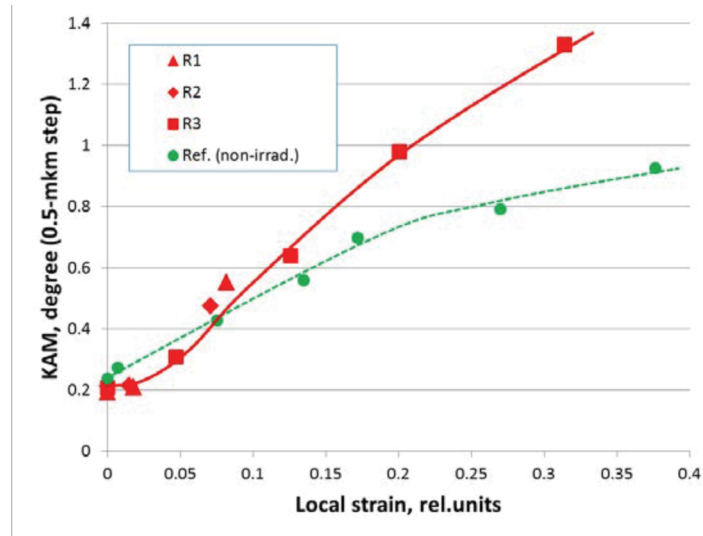
**Figure 39. KAM as a function of local plastic strain level for
irradiated and reference specimens (step size = 0.5 μm).**

Figure 39 shows the KAM(ε) curves for reference and irradiated specimens. One can see that the results for the reference material agree well with the literature [19,33]. There is a close-to-linear relationship between KAM and strain level for strains below ~0.2; KAM monotonously increases with strain up to ~0.2 and after that tends to saturate.

In contrast, the irradiated steel KAM values show very weak changes in the small strain area (0–0.03) and after that quickly increase. Small strains were not visible in the average KAM plot. Most likely, during EBSD scanning the electron beam probed mostly nondeformed material but not narrow (~40-50) nm channels. The surface fraction of hot spots was too small to cause visible changes in KAM at small strains. Interestingly, as stress increased, KAM values for the irradiated specimen increased much faster compared to the reference nonirradiated one. Assuming changes in KAM values reflect the change in dislocation (i.e., strain-induced defects) density, one could speculate that defect density increases faster in irradiated steel compared to nonirradiated steel.

5.   SUMMARY AND CONCLUSIONS

In the present work, an advanced in situ SEM-EBSD mechanical test approach was implemented at the ORNL's LAMDA facility to test irradiated specimens of LWR-relevant steels and alloys. The in situ test method is now available for the LWRS program, its collaborators, and other users. A miniature tensile frame with a 5 kN loading capacity may be installed inside the VERSA 3D SEM, equipped with EBSD, EDS, and FIB capabilities. The frame allows for both tension and compression modes and has a heating stage that provides temperatures up to 800°C. Designing custom grips will enable the tensile frame to accommodate most common mechanical test methods, including tensile, compression, and fracture mechanics testing. This development, coupled with LAMDA's ability to handle irradiated materials and produce specimens from radioactive objects, provides a set of unique experimental opportunities.

Limited testing was conducted using nonirradiated 304L steel—a reference material for irradiated specimens already available at LAMDA—to validate the method and provide baseline data for further analysis. The tests confirmed the possibility to track, scan, and investigate the selected area and analyze strain-induced phenomena including grain rotation, changes in the local misorientation, slip line development, appearance, and evolution of strain-induced twins.

The pilot SEM-EBSD in situ test with irradiated material demonstrated that dislocation channels might form at ~0.5 yield stress at conventional strain rate ($10^{-3}s^{-1}$); misorientation level (GROD value) increased much faster in the irradiated material compared to the reference alloy. Deformation localization led to the formation of the specific hot spots with high local misorientation. Such hot spots may have different corrosion behavior in the high-temperature water promoting localized corrosion damage and stress corrosion crack initiation.

Additionally, a test with irradiated specimen was conducted at the SNS VULCAN facility, yielding results on strain/stress partitioning between grains of different families, retained stresses, diffraction peak broadening, and defect density evolution. It was demonstrated that pronounced increase in the defect density occurred after loading at ~0.9 of yield stress. If funding permits, the same irradiated material will be tested using the SEM-EBSD approach, bridging these important methods.

Future activity will include SEM-EBSD tensile testing of the irradiated specimens at LWR-relevant temperature ranges, testing of highly irradiated specimens (up to 120 dpa) and advanced testing with slow strain rate. Several methodical issues such as the long-term stability of the system at high temperature may need to be addressed; however, if the equipment permits, the goal is to reach a strain rate of $10^{-7}s^{-1}$. Once the strain localization areas are identified and deformation localization mechanisms are well enough understood, the local corrosion behavior and stress corrosion crack initiation and growth mechanisms in the irradiated austenitic steel – materials of light water reactors – will be examined via in-situ electro-chemical microscopy. This method is under development at the University of California Los-Angeles (Dr. G. Sant) within the framework of LWRS program.

6.   ACKNOWLEDGMENTS

7.   REFERENCES

[1]   K. Fukuya, "Current understanding of radiation-induced degradation in light water reactor structural materials," *Journal of Nuclear Science and Technology*, vol. 50, 2013, pp. 213–254.

[2]   K. Fukuya, M. Nakano, K. Fujii, and T. Torimaru, "IASCC susceptibility and slow tensile properties of highly-irradiated 316 stainless steels," *Journal of nuclear science and technology*, vol. 41, 2004, pp. 673–681.

[3]   Z. Jiao and G. Was, "Impact of localized deformation on IASCC in austenitic stainless steels," *Journal of Nuclear Materials*, vol. 408, 2011, pp. 246–256.

[4]   G.S. Was, Y. Ashida, and P.L. Andresen, "Irradiation-assisted stress corrosion cracking," *Corrosion Reviews*, vol. 29, 2011, pp. 7–49.

[5]   K.G. Field, M.N. Gussev, and J.T. Busby, "Microstructural characterization of deformation localization at small strains in a neutron-irradiated 304 stainless steel," *Journal of Nuclear Materials*, vol. 452, 2014, pp. 500–508.

[6]   M.N. Gussev, K.G. Field, and J.T. Busby, "Strain-induced phase transformation at the surface of an AISI-304 stainless steel irradiated to 4.4 dpa and deformed to 0.8% strain," *Journal of Nuclear Materials*, vol. 446, 2014, pp. 187–192.

[7]   M. McMurtrey, G. Was, L. Patrick, and D. Farkas, "Relationship between localized strain and irradiation assisted stress corrosion cracking in an austenitic alloy," *Materials Science and Engineering: A*, vol. 528, 2011, pp. 3730–3740.

[8]   C. Boehlert, S. Longanbach, M. Nowell, and S. Wright, "The evolution of grain-boundary cracking evaluated through in situ tensile-creep testing of Udimet alloy 188," *Journal of Materials Research*, vol. 23, 2008, pp. 500–506.

[9]   A. Clair, M. Foucault, O. Calonne, Y. Lacroute, L. Markey, M. Salazar, V. Vignal, and E. Finot, "Strain mapping near a triple junction in strained Ni-based alloy using EBSD and biaxial nanogauges," *Acta Materialia*, vol. 59, 2011, pp. 3116–3123.

[10] T. Britton, J. Jiang, R. Clough, E. Tarleton, A. Kirkland, and A. Wilkinson, "Assessing the precision of strain measurements using electron backscatter diffraction–Part 2: experimental demonstration," *Ultramicroscopy*, vol. 135, 2013, pp. 136–141.

[11] P. Scott, "Materials reliability program: a review of the cooperative irradiation assisted stress corrosion cracking research program (MRP-98)," *EPRI Report*, vol. 1002807, 2003.

[12] J. Massoud, P. Dubuisson, P. Scott, and V. Chamardine, "CIR II program: description of the Boris 6 and 7 experiments in the BOR-60 fast breeder reactor," *EPRI Report*, vol. 1011787, 2005.

[13] M. Ojima, J. Inoue, S. Nambu, P. Xu, K. Akita, H. Suzuki, and T. Koseki, "Stress partitioning behavior of multilayered steels during tensile deformation measured by in situ neutron diffraction," *Scripta Materialia*, vol. 66, 2012, pp. 139–142.

[14] C. Tomchik, J. Almer, O. Anderoglu, L. Balogh, D.W. Brown, B. Clausen, S.A. Maloy, T.A. Sisneros, and J.F. Stubbins, "High energy X-ray diffraction study of the relationship between the macroscopic mechanical properties and microstructure of irradiated HT-9 steel," *Journal of Nuclear Materials*, vol. 475, 2016, pp. 46–56.

[15] V.I. Voronin, E.Z. Valiev, I.F. Berger, B.N. Goschitskii, N.V. Proskurnina, V.V. Sagaradze, and N.F. Kataeva, "Neutron diffraction analysis of Cr–Ni–Mo–Ti austenitic steel after cold plastic deformation and fast neutrons irradiation," *Journal of Nuclear Materials*, vol. 459, 2015, pp. 97–102.

[16]   J.-Y. Buffiere, E. Maire, J. Adrien, J.-P. Masse, and E. Boller, "In situ experiments with X ray tomography: an attractive tool for experimental mechanics," *Experimental mechanics*, vol. 50, 2010, pp. 289–305.

[17]   M. Chen, D. Terada, A. Shibata, and N. Tsuji, "Identical Area Observations of Deformation-Induced Martensitic Transformation in SUS304 Austenitic Stainless Steel," *MATERIALS TRANSACTIONS*, vol. 54, 2013, pp. 308–313.

[18]   Y.B. Das, A.N. Forsey, T.H. Simm, K.M. Perkins, M.E. Fitzpatrick, S. Gungor, and R.J. Moat, "In situ observation of strain and phase transformation in plastically deformed 301 austenitic stainless steel," *Materials & Design*, vol. 112, 2016, pp. 107–116.

[19]   M. KAMAYA, K. KUBUSHIRO, Y. SAKAKIBARA, S. SUZUKI, H. MORITA, R. YODA, D. KOBAYASHI, K. YAMAGIWA, T. NISHIOKA, Y. YAMAZAKI, and others, "Round robin crystal orientation measurement using EBSD for damage assessment," *Mechanical Engineering Journal*, vol. 3, 2016, pp. 16–77.

[20]   J. Jiang, T.B. Britton, and A.J. Wilkinson, "Evolution of dislocation density distributions in copper during tensile deformation," *Acta Materialia*, vol. 61, 2013, pp. 7227–7239.

[21]   P.S. Karamched and A.J. Wilkinson, "High resolution electron back-scatter diffraction analysis of thermally and mechanically induced strains near carbide inclusions in a superalloy," *Acta Materialia*, vol. 59, 2011, pp. 263–272.

[22]   V. Mertinger, E. Nagy, F. Tranta, and J. Sólyom, "Strain-induced martensitic transformation in textured austenitic stainless steels," *Materials Science and Engineering: A*, vol. 481, 2008, pp. 718–722.

[23]   M.N. Gussev, J.T. Busby, T.S. Byun, and C.M. Parish, "Twinning and martensitic transformations in nickel-enriched 304 austenitic steel during tensile and indentation deformations," *Materials Science and Engineering: A*, vol. 588, 2013, pp. 299–307.

[24]   R.W. Bosch, M. Vankeerberghen, R. Gérard, and F. Somville, "Crack initiation testing of thimble tube material under PWR conditions to determine a stress threshold for IASCC," *Journal of Nuclear Materials*, vol. 461, 2015, pp. 112–121.

[25]   B. Margolin, A. Sorokin, V. Shvetsova, A. Minkin, V. Potapova, and V. Smirnov, "The radiation swelling effect on fracture properties and fracture mechanisms of irradiated austenitic steels. Part I. Ductility and fracture toughness," *Journal of Nuclear Materials*, vol. 480, 2016, pp. 52–68.

[26]   S. Jeong, U. Kang, J. Choi, and W. Nam, "Comparative Study of Hardening Mechanisms During Aging of a 304 Stainless Steel Containing α' -Martensite," *Journal of materials engineering and performance*, vol. 21, 2012, pp. 1937‑1942.

[27]   M. Gusev, O. Maksimkin, I. Osipov, and F. Garner, "Anomalously large deformation of 12Cr18Ni10Ti austenitic steel irradiated to 55dpa at 310° C in the BN-350 reactor," *Journal of Nuclear Materials*, vol. 386, 2009, pp. 273–276.

[28]   M.N. Gussev, K.G. Field, and J.T. Busby, "Deformation localization and dislocation channel dynamics in neutron-irradiated austenitic stainless steels," *Journal of Nuclear Materials*, vol. 460, 2015, pp. 139–152.

[29]   L. Zhang, S. Takahashi, Y. Kamada, H. Kikuchi, K. Ara, M. Sato, and T. Tsukada, "Magnetic properties of SUS 304 austenitic stainless steel after tensile deformation at elevated temperatures," *Journal of materials science*, vol. 40, 2005, pp. 2709–2711.

[30]   M. Gussev, J. Busby, K. Field, M. Sokolov, and S. Gray, "Role of scale factor during tensile testing of small specimens," *Small Specimen Test Techniques: 6th Volume*, ASTM International, 2015.

[31] S. Kahl, R.L. Peng, M. Calmunger, B. Olsson, and S. Johansson, "In situ EBSD during tensile test of aluminum AA3003 sheet," *Micron*, vol. 58, 2014, pp. 15–24.

[32] G. Winther, L. Margulies, S. Schmidt, and H. Poulsen, "Lattice rotations of individual bulk grains Part II: correlation with initial orientation and model comparison," *Acta Materialia*, vol. 52, 2004, pp. 2863–2872.

[33] M. Kamaya, "Assessment of local deformation using EBSD: Quantification of local damage at grain boundaries," *Materials characterization*, vol. 66, 2012, pp. 56–67.

[34] M. Kamaya, A.J. Wilkinson, and J.M. Titchmarsh, "Quantification of plastic strain of stainless steel and nickel alloy by electron backscatter diffraction," *Acta Materialia*, vol. 54, 2006, pp. 539–548.

[35] X.-L. Wang, T. Holden, G.Q. Rennich, A. Stoica, P.K. Liaw, H. Choo, and C.R. Hubbard, "VULCAN—The engineering diffractometer at the SNS," *Physica B: Condensed Matter*, vol. 385, 2006, pp. 673–675.

[36] X.-L. Wang, T.M. Holden, A.D. Stoica, K. An, H.D. Skorpenske, A. Jones, G. Rennich, and E. Iverson, "First results from the VULCAN diffractometer at the SNS," *Materials Science Forum*, Trans Tech Publ, 2010, pp. 105–110.

[37] X.-L. Wang and A. Stoica, "Focusing neutron guides for VULCAN—Design aspects, estimated performance, and detector deployment," *Nuclear Instruments and Methods in Physics Research Section A: Accelerators, Spectrometers, Detectors and Associated Equipment*, vol. 600, 2009, pp. 309–312.

[38] G.M. Stoica, A.D. Stoica, K. An, D. Ma, S. Vogel, J. Carpenter, and X.-L. Wang, "Extracting grain-orientation-dependent data from in situ time-of-flight neutron diffraction. I. Inverse pole figures," *Journal of Applied Crystallography*, vol. 47, 2014, pp. 2019–2029.

[39] K. An and V. Reduction, "Interactive Visualization Software for Event Mode Neutron Diffraction, ORNL Report, Oak Ridge National Laboratory," *ORNL-TM-2012-621*, 2012.

[40] A.C. Larson and R.B. Von Dreele, "Gsas," *General Structure Analysis System. LANSCE, MS-H805, Los Alamos, New Mexico*, 1994.

[41] P. Thompson, D. Cox, and J. Hastings, "Rietveld refinement of Debye–Scherrer synchrotron X-ray data from Al2O3," *Journal of Applied Crystallography*, vol. 20, 1987, pp. 79–83.

[42] J.A. Simmons, R. Bullough, and R. De Wit, *Fundamental aspects of dislocation theory: conference proceedings*, National Bureau of Standards, 1970.